Unraveling the host-selective toxic interaction of cassiicolin with lipid membranes and its cytotoxicity

Key words: Lipid membranes, host-selective toxin, cassiicolin, *Corynespora cassiicola*, biofilm, HS-AFM

Running title: Host-selective toxic interaction of cassiicolin with lipids

Kien Xuan Ngo[1#*], Nguyen Bao Quoc[2#*], Phuong Doan N. Nguyen[1,2], Hirotoshi Furusho[1], Makoto Miyata[3], Tomomi Shimonaka[3], Nguyen Ngoc Bao Chau[4], Nguyen Phuong Vinh[5], Nguyen Anh Nghia[5], Tareg Omer Mohammed[1], Takehiko Ichikawa[1], Noriyuki Kodera[1], Hiroki Konno[1], Takeshi Fukuma[1], Toshio Ando[1]

Affiliations

[1]Nano Life Science Institute (WPI-NanoLSI), Kanazawa University, Kakuma-machi, Kanazawa, Japan.

[2]Research Institute for Biotechnology and Environment, Nong Lam University, Ho Chi Minh City, Vietnam.

[3]Department of Biology, Graduate School of Science, Osaka City University, Osaka, Japan.

[4]Faculty of Biotechnology, Ho Chi Minh City Open University, Ho Chi Minh City, Vietnam.

[5]Rubber Research Institute of Vietnam, Ho Chi Minh City, Vietnam.

Corresponding authors (*)

Kien Xuan Ngo (ngoxuankien@staff.kanazawa-u.ac.jp)

Nguyen Bao Quoc (baoquoc@hcmuaf.edu.vn)

[#]These authors contributed equally.

Graphic Abstract

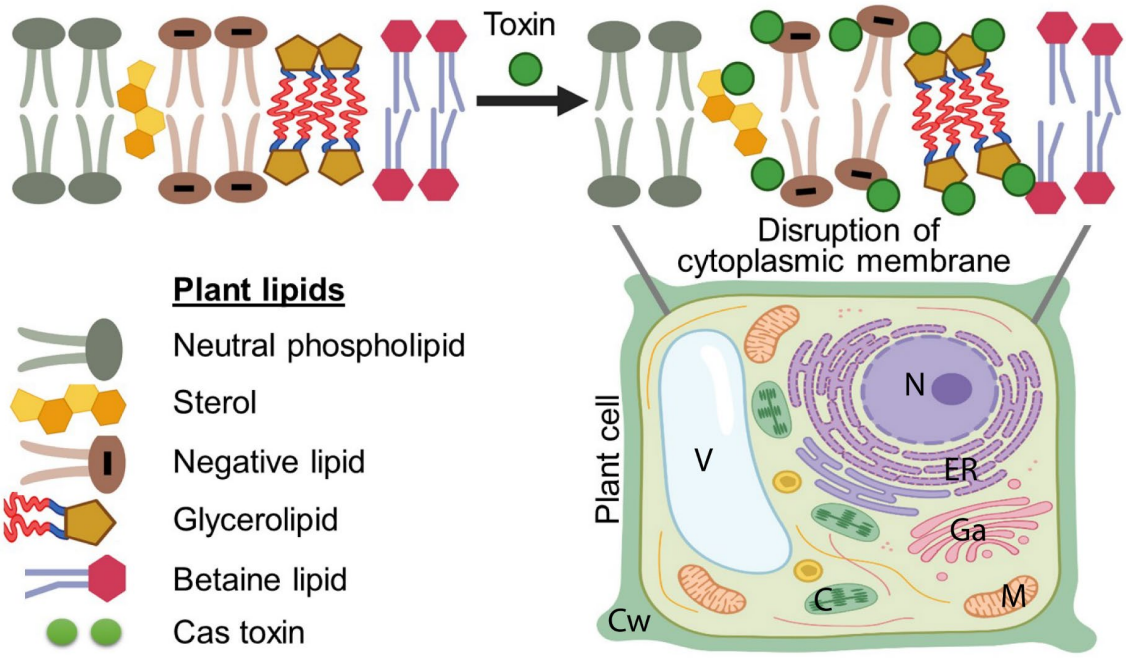

Highlights

- Cas1 and Cas2 directly damage and cause necrosis in the leaves of specific rubber clones.
- Cas1 and Cas2 can form biofilm-like structures on specific lipid membranes (negative phospholipids, glycerolipids, and sterols). The biofilm-like formation of Cas toxin plays an important role in selective disruption on lipid membranes.
- Vulnerability of the specific cytoplasmic membranes to the selective Cas toxin that is the most remarkable feature of cytotoxicity of Cas toxin on plant cells.

Abstract

Cassiicolin (Cas), a toxin produced by *Corynespora cassiicola*, is responsible for corynespora leaf fall disease in rubber trees. Currently, the molecular mechanism of the cytotoxicity of Cas and its host selectivity have not been fully elucidated. Here, we analyzed the binding of Cas1 and Cas2 to membranes consisting of different plant lipids and their membrane-disruption activities. Using high-speed atomic force microscopy and confocal microscopy, we reveal that the binding and disruption activities of Cas1 and Cas2 on lipid membranes are strongly dependent on the specific plant lipids. The negative phospholipids, glycerolipids, and sterols are more susceptible to membrane damage caused by Cas1 and Cas2 than neutral phospholipids and betaine lipids. Cytotoxicity tests on rubber leaves of RRIV 1, RRIV 4, and PB 255 clones suggest that the toxins cause necrosis of rubber leaves, except for the strong resistance of PB 255 against Cas2. Cryo-SEM analyses of necrotic leaf tissues exposed to Cas1 confirm that cytoplasmic membranes are vulnerable to the toxin. Thus, the host selectivity of Cas toxin is attained by the lipid-dependent binding activity of Cas to the membrane, and the cytotoxicity of Cas arises from its ability to form biofilm-like structures and disrupt specific membranes.

Introduction

The necrotrophic fungus *Corynespora cassiicola* (Berk.&Curt) Wei is a causal pathogen of corynespora leaf fall (CLF) disease in rubber leaves, of which the typical symptoms are brown leaf lesions surrounded by a yellow halo and occasional blackening of the veins, which causes a symptomatic “fish-bone” appearance, resulting in massive defoliation in susceptible rubber clones (Ribeiro et al., 2019). *C. cassiicola* predominantly infects both young and mature leaves, and CLF disease has now become widespread in *Hevea brasiliensis* plantations, causing severe damage to the natural rubber industry. These pathogens have also been found in many other crops (Dixon et al., 2009; Shrestha et al., 2017; Sumabat et al., 2018). Although the first pathogenic *C. cassiicola* isolate originally from the Philippines (CCP) is described as a causal agent in CLF disease, a necrotrophic effector known as cassiicolin (Cas) toxin produced in CCP is widely accepted as the host-selective toxin (HST) interaction in rubber trees and other plants (Barthe et al., 2007; de Lamotte et al., 2007; Déon et al., 2014, 2012a; Ribeiro et al., 2019; Wu et al., 2018). The Cas-encoding genes were found to be transiently expressed one or two days post inoculation, suggesting a role of Cas toxin in the early phase of infection (Déon et al., 2012a). Cas toxin is a small glycosylated secreted protein effector associated with secondary metabolism in *C. cassiicola* (Barthe et al., 2007; de Lamotte et al., 2007; Déon et al., 2014, 2012a). To date, six cassiicolin isoforms (Cas1 to Cas6) have been

genetically identified by PCR-based detection from fungal isolates in various host plants and geographical origins (Déon et al., 2014, 2012a). Of note, *C. cassiicola* isolates only carry and express specific Cas genes, depending on the host specialization (Déon et al., 2014; Hieu et al., 2020; Lopez et al., 2018; Nghia et al., 2008; Nguyen et al., 2014). Some *C. cassiicola* isolates possessing no Cas gene yet causing CLF diseases may reveal other putative effectors involved (Lopez et al., 2018). The nature of the HST interaction of Cas toxin in CLF disease remains controversial because *in silico* analysis and prediction revealed 2870 putative effectors comprising CaZymes, lipases, peptidases, and secreted proteins and enzymes associated with secondary metabolism of *C. cassiicola* (Lopez et al., 2018). However, recent studies reported that gene deletion of Cas1 in *C. cassiicola* completely suppresses fungal pathogenicity in rubber trees (Ribeiro et al., 2019; Tran et al., 2016). These studies suggested two important findings: (i) Cas1 is a necrotrophic effector conferring virulence to *C. cassiicola* in susceptible rubber clones; (ii) other effectors produced in *C. cassiicola* contribute to residual filtrate toxicity and virulence in senescing/wounded tissues. Thus, the putative effectors may be involved in saprotrophs rather than necrotrophs. However, the cytotoxicity of Cas2 on rubber leaves has never been clarified before and remains unknown. Of special interest, we further examined and clarified the cytotoxicity of Cas isoforms (i.e., Cas1 and Cas2) to understand the fundamental molecular mechanisms underlying the HST interaction of Cas toxin in leaves of various rubber clones. In this context, the direct cytotoxicity of Cas1 to rubber leaves has been explored in some previous studies (Barthe et al., 2007; de Lamotte et al., 2007; Déon et al., 2012b). Notably, purified Cas1 applied on rubber leaves caused the same symptoms as *C. cassiicola* did at the cellular level (Barthe et al., 2007; de Lamotte et al., 2007). Electron microscopic analyses of necrotic leaf tissues revealed that Cas1 severely damaged plasma membranes in the chloroplast. Similarly, AK toxins from *Alternaria kikuchiana* and fumonisins and AAL toxin from *Fusarium* species infecting crops and plants were also reported to severely damage cytoplasmic membranes in various ways (Meena and Samal, 2019; Park et al., 1976; Riley et al., 1996; Tsuge et al., 2013). Objectively, no study has sufficiently clarified the susceptibility of plant lipids such as phospholipids, glycerolipids, sterols, and betaine lipids (Bae et al., 2020; Dörmann and Benning, 2002; Dufourc, 2008a, 2008b; Hartmann, 1998; Liengprayoon et al., 2011; Mackender and Leech, 1974; Murakami et al., 2018; Poincelot, 1976) to the pathogenicity of Cas toxin.

Alternatively, plant resistance to infectious diseases is also known to be associated with several defense responses activated by host-pathogen interactions (Thatcher et al., 2005). Recent transcriptomic analyses of the genetic responses of rubber clones

susceptible and tolerant to *C. cassiicola* explored the diversity of genes encoding disease resistance proteins, leucine-rich repeat proteins, and genes involved in carbohydrate metabolic processes that were significantly upregulated in tolerant rubber clones upon infection. These genes, however, were either completely suppressed or downregulated in susceptible rubber clones (Roy et al., 2019). Again, molecular phylogenetic studies failed to determine the key factor in the host selectivity of Cas toxin. The nature of the HST interaction of Cas toxin in CLF disease in different rubber clones remains elusive.

This study addressed several key questions to elucidate the HST interaction of Cas toxin with plant lipids and its cytotoxicity on rubber leaves. Specifically, we examined the susceptibility of several important lipid components in plants to the pathogenicity of Cas1 and Cas2 isoforms at the molecular and cellular levels by combining high-speed atomic force microscopy (HS-AFM), confocal microscopy, and cryo-scanning electron microscopy (Cryo-SEM), thereby clarifying the HST interaction of Cas1 and Cas2 isoforms to different plant lipids. At the cellular level, we examined the cytotoxicity of Cas1 and Cas2 on rubber leaves of RRIV 1, RRIV 4, and PB 255 clones to understand the HST interaction of Cas isoforms to specific hosts. Here, we report that the binding and disruption activities of Cas1 and Cas2 are more sensitive to negatively charged lipids (DPPA), glycerolipids (MGDG, DGDG), and sterols (stigmasterol, sitosterol) than to neutral (DPPC) and betaine lipids (DGTS-d9, DGTS). Cas toxins could form biofilm-like structures onto specific lipid membranes composed of negative phospholipid, glycerolipids, and sterols, but failed to form these structures onto the membranes composed of betaine lipids (e.g., DGTS-d9). Cytotoxicity tests of Cas1 and Cas2 on rubber leaves of RRIV 1, RRIV 4, and PB 255 clones suggest that these clones are highly susceptible to the pathogenicity of Cas1 and Cas2 except for the strong resistance of PB 255 against Cas2. Finally, we also report that cytoplasmic membranes in susceptible rubber clones are highly vulnerable to the pathogenicity of purified Cas toxin and toxin produced from fungus *C. cassiicola*.

Results

Disruption activity of Cas1 and Cas2 to different lipid membranes imaged by HS-AFM

To examine the possible pathogenicity of Cas1 and Cas2, this study addressed the first question of whether Cas1 and Cas2 could bind to and disrupt various phospholipids (DPPC, DPPA), glycerolipids (MGDG, DGDG), sterols (stigmasterol, sitosterol), and betaine lipids (DGTS-d9, DGTS) available in plants. To answer this question, we used tapping-mode HS-AFM to image the dynamic interaction and disruption activities of

167 Cas1 and Cas2 to different lipid membranes in real time. Unlike a conventional AFM,
168 which has a slow scanning rate, HS-AFM can image in sub-second temporal resolution
169 many biological molecules during functional activities (Ando, 2012; Ando et al., 2013,
170 2008, 2007; Uchihashi et al., 2012). The very soft and small cantilever used in HS-AFM
171 was proven in numerous previous reports to non-invasively perturb the structures and
172 functions of biological molecules (Kodera et al., 2010; Lin et al., 2020; Ngo et al., 2015;
173 Uchihashi et al., 2011). This microscopy enables real-time, high-resolution imaging of
174 individual biological nanomachines during their functional activities, as demonstrated by
175 studies on walking myosin V (Kodera et al., 2010), rotorless F1-ATPase (Uchihashi et al.,
176 2011), and actin filaments interacting with cofilin (Ngo et al., 2015), and recently explores
177 many undiscovered features of many other inspired biomolecules (Ando, 2018; Heath
178 and Scheuring, 2019; Karner et al., 2017; Kodera et al., 2020; Lin et al., 2020; Nasrallah
179 et al., 2019; Shibata et al., 2017).
180 We produced Cas1 and Cas2 recombinant proteins in *E. coli*. The basic characteristics
181 of these proteins are described in **Figure 1-figure supplements 1, 2, and Figure 1-tables**
182 **1, 2**. Our analysis predicted that a signal peptide (SP) domain in Cas1 and Cas2 containing
183 several different hydrophobic amino acids (M, Y, L, I, A, F, V) may help to better insert
184 these proteins into the hydrophobic region of a lipid bilayer. The numbers of negatively
185 and positively charged residues in Cas1 and Cas2 are identical. However, the secondary
186 structures (α-helix, β-sheet, and β-turn) in the mature domains of Cas1 and Cas2 are
187 locally different (see red and yellow rectangles in **Figure 1-figure supplement 1**). To
188 follow the binding and disruption activities of Cas1 and Cas2 on preformed lipid
189 membranes in solution, Cas1 or Cas2 was added into the imaging chamber at a final
190 concentration of 0.95 μM during HS-AFM imaging. Initially, we found that neutral
191 phospholipid (DPPC) membranes were weakly sensitive to the binding and disruption
192 activities of Cas1 and Cas2 (**Figures 1a1, a2, d-a1, d-a2, Figure 1-figure supplement 3,**
193 **Table 1, and Videos 1 – 2**). Thus, we made several composite lipid membranes by mixing
194 with DPPC lipids to investigate their susceptibility to the pathogenicity of Cas1 and Cas2.
195 As shown in **Figures 1b1, d-b1, c1, d-c1, d1, d-d1, b2, d-b2, c2, d-c2, d2, and d-d2,**
196 **Table 1, and Videos 3 – 8**, the negatively charged phospholipid (DPPC/DPPA) and
197 glycerolipid (DPPC/MGDG, DPPC/DGDG) mixtures were highly sensitive to the
198 binding and disruption activities of Cas1 and Cas2. The DPPC/stigmasterol and
199 DPPC/sitosterol membranes were also strongly susceptible to the binding and disruption
200 activities of both Cas1 and Cas2 (**Figures 1e1, d-e1, e2, d-e2, f1, d-f1, f2, and d-f2, Table**
201 **1, and Videos 9 – 12**). The lipid membrane mixtures of betaine lipids (DPPC/DGTS-d9,
202 DPPC/DGTS) were weakly vulnerable to Cas1 and Cas2 (**Figures 1g1, d-g1, h1, d-h1,**

g2, d-g2, h2, and d-h2, Table 1, and Videos 13 – 16).

In this study, our real-time HS-AFM imaging Videos revealed that Cas1 and Cas2 were strongly bound to membranes containing negatively charged phospholipid (DPPA), glycerolipids (MGDG, DGDG), and sterols (stigmasterol, sitosterol) and penetrated deeply into the lipid membranes. Cas1 and Cas2 formed large clusters on these highly susceptible membrane lipids and expanded their clusters, similar to tsunamis, to devastate the membranes (**Figures 1b1, b2, c1, c2, d1, d2, e1, e2, f1, and f2, and Videos 3 – 10**). By acting in these ways, they continuously damage lipid membranes. After disruption, many aggregates left on mica were observed. These aggregates were likely a mixture composed of lipids and Cas1 or Cas2. Our results also show that neutral DPPC lipids were weakly susceptible to the binding and disruption activity of both Cas1 and Cas2 (**Figures 1a1, d-a1, a2, d-a2, and Videos 1 – 2**). This statement is firmly supported in the observation of the disruption activity of Cas1 and Cas2 to DPPC domains and DGDG domains segregated in DPPC/DGDG membranes (**Figure 2B, 2D, and Videos 7 – 8**). The DPPC and DGDG lipid domains formed on the mica surface were distinguished by a height difference of ~1.5 – 1.9 nm. Cas clusters were also distinguished by measuring the height differences with membranes and are representatively shown for Cas1 and Cas2 clusters (**Figure 2**). DGDG domains were strongly devastated by Cas1 and Cas2 clusters, while DPPC domains remained almost intact (kymographs in **Figures 2E and 2F**). Based on this observation, we further confirmed that glycerolipids (MGDG, DGDG) are strongly susceptible to the disruption activity of Cas1 and Cas2. Most likely, the negatively charged surface and high membrane fluidity of glycerolipids are two key factors for better binding, accessibility, and damage activity of Cas1 and Cas2 clusters in these membranes. We further tested membrane accessibility for the disruption activity of Cas1 and Cas2 by incorporating sterols (stigmasterol, sitosterol) into the membranes. The presence of plant sterols in membranes was expected to increase the membrane accessibility for Cas1 and Cas2, although sterols are generally thought to decrease the membrane fluidity (Dufourc, 2008a, 2008b). Indeed, these membranes were greatly devastated by Cas1 and Cas2. The disruption activities of Cas toxin on these membranes happened regardless of the Cas cluster formation or not (**Figures 1e1, d-e1, e2, d-e2, f1, d-f1, f2, and d-f2 and Videos 9 – 12**). Additionally, when neutral betaine lipids (DGTS-d9, DGTS) were mixed with DPPC lipids, these membranes were only weakly damaged by Cas1 and Cas2. The degrees of damage of Cas1 and Cas2 on these membranes were similar to those on pure DPPC membranes (**Figures 1a1, d-a1, a2, d-a2, g1, d-g1, g2, d-g2, h1, d-h1, h2, and d-h2, and Videos 1 – 2, 13 – 16)**. Overall, we suggest that negatively charged phospholipids, glycerolipids, and specific sterols available in the

239 cytoplasmic membranes of plant cells are strongly sensitive to the disruption activity of
240 Cas1 and Cas2. Neutral phospholipids and betaine membrane lipids are weakly
241 susceptible to the disruption activity of Cas1 and Cas2.
242
243 **Biofilm-like formation of Cas toxin onto specific lipid membranes**
244 To examine whether biofilm-like structures of Cas toxin could be formed on specific
245 lipid membranes, we used HS-AFM and imaged in realtime the binding of Cas toxin to
246 the preformed lipid membranes in solution. Generally, the formation of the infectious
247 microbial biofilms plays various important roles such as tolerance to the host immune
248 system, cell adhesion, serve as a reservoir for cell division (Mancera et al., 2020), and
249 nutritive absorption, protective barrier, development of reproductive and vegetative
250 structures (i.e., fungal spore and hyphae), and sexual and asexual reproduction (Gour et
251 al., 2014; Siqueira and Lima, 2013).
252 In this study, we used a high concentration of Cas1 and Cas2 (4.75 μM) and compared
253 the biofilm-like formation of Cas toxin on two different lipid membrane surfaces (i.e., the
254 susceptible DPPC/sitosterol vs. the non-susceptible DPPC/DGTS-d9 membranes). We
255 found that the lipid membranes composed of DPPC/sitosterol strongly recruited the
256 binding and biofilm-like formation of the Cas1/Cas2 mixture (**Figure 3A, Video 17**). The
257 biofilm of the Cas1/Cas2 mixture was covered and partially incorporated onto membranes.
258 The biofilm thickness of the Cas1/Cas2 mixture was approximately 5 – 6.5 nm, and its
259 height protruded over the membrane surface was ~1 – 1.5 nm (**Figure 3A**). Consequently,
260 the disruption activities of the Cas1/Cas2 mixture on these membranes were very strong
261 (**Figure 3A, Video 17**). These membranes also recruited the biofilm-like formation of
262 Cas2. The biofilm-like structures of Cas2 were covered on the membrane surface with a
263 thickness of ~0.3 – 0.5 nm (**Figure 3B, Video 18).** Contrarily, the lipid membranes made
264 of DPPC/DGTS-d9 failed to form the biofilm-like structures of the Cas1/Cas2 mixture.
265 Despite a combination of Cas1 and Cas2 at a high concentration, the Cas1/Cas2 clusters
266 were partially incorporated into membranes and yet weakly disrupted these membranes
267 (**Figure 3C, Video 19**). Additionally, Cas1 and Cas2 at a lower concentration (~0.95 μM)
268 could also form biofilm-like structures on membranes containing negative phospholipid
269 (DPPC/DPPA) (**Figures 1b1, b2, Videos 3 – 4**) and glycerolipid (DPPC/DGDG)
270 (**Figures 1d1, d2, Videos 7 – 8**). Biofilm-like formation of Cas1 was also seen on
271 membranes containing glycerolipid (DPPC/MGDG) (**Figure 1c1, Video 5**). We suggest
272 here, for the first time, that biofilm-like structures of Cas toxin can be formed onto
273 specific lipid membranes available in plant cells (i.e., negative phospholipid,
274 glycerolipids, and sterol). The effective biofilm-like formation of the Cas1/Cas2 mixtures

275 onto specific lipid membranes may also reflect the nature of Cas toxin production and
276 virulence of *C. cassiicola* possessing various Cas isoforms when they infect and grow on
277 rubber leaves.
278
279 **Binding of Cas1 and Cas2 to artificial cytoplasmic membranes imaged by confocal**
280 **microscopy**
281 We further examined the susceptibility of intact lipid membranes to the binding of
282 Cas1 and Cas2 using confocal microscopy. Thus, we fabricated giant liposome vesicles
283 (GVs) and used them as a model of artificial cytoplasmic membranes to assay the binding
284 activities of GFP-Cas1 and GFP-Cas2 using confocal microscopy, a powerful technique
285 to study protein-lipid membrane interaction (Carvalho et al., 2008; Drücker et al., 2019).
286 The composite GVs composed of similar lipid compositions used in HS-AFM
287 observation were made by electroformation methods (**Figure 1-figure supplement 3 and**
288 **Figure 4-table 1**). Here, we mainly compared the binding of GFP-Cas1 and GFP-Cas2
289 to different GVs made of DPPC, DPPC/DPPA, DPPC/MGDG, DPPC/DGDG,
290 DPPC/stigmasterol, DPPC/sitosterol, DPPC/DGTS-d9, and DPPC/DGTS lipid mixtures
291 with the small addition of rhodamine-PE and biotinyl-PE lipids to absorb and image GVs.
292 Principally, we fabricated GVs containing both giant unilamellar and multilamellar
293 vesicles and used them to assay the binding activity of GFP-Cas1 and GFP-Cas2 (**Figure**
294 **4, Tables 1, 2**). The binding of GFP-Cas1 and GFP-Cas2 to GVs made of only neutral
295 phospholipids (DPPCs) was indeed weak (**Figures 4a1, a2, i1, i2**). Most DPPC GVs were
296 not bound with GFP-Cas1 and GFP-Cas2. Thus, we used DPPC as the basal lipid
297 membrane to compare the binding degrees of GFP-Cas1 and GFP-Cas2 to GVs composed
298 of negative phospholipids (DPPC/DPPA), glycerolipids (DPPC/MGDG, DPPC/DGDG),
299 sterols (DPPC/stigmasterol, DPPC/sitosterol), and neutral betaine lipids (DPPC/DGTS-
300 d9, DPPC/DGTS). GFP-Cas1 was bound more strongly to GVs composed of
301 DPPC/DPPA, DPPC/MGDG, and DPPC/DGDG lipids than to GVs made of only DPPC
302 (**Figures 4a1, b1, c1, d1, i1**). The susceptibility of GVs composed of DPPC/stigmasterol,
303 DPPC/sitosterol, DPPC/DGTS-d9, and DPPC/DGTS lipids to the binding of GFP-Cas1
304 was also recorded as strong (**Figures 4e1, f1, g1, h1**), although when compared to the
305 binding of GFP-Cas1 to GVs made of only DPPC (**Figure a1**), the difference ($p \leq 0.05$,
306 *t-test*) was not significant (**Figure 4i1, Table 2**). Additionally, we found that GFP-Cas2
307 bound more strongly to all GVs composed of the negative phospholipids, glycerolipids,
308 sterols, and betaine lipids used in this study compared to GVs made of only the neutral
309 DPPC phospholipids (**Figures 4a2, b2, c2, d2, e2, f2, g2, h2, i2**). These results strongly
310 support that both GFP-Cas1 and GFP-Cas2 were bound to suspended lipid membranes,

311 similar to artificial cytoplasmic membranes composed of the specific plant lipids. The
312 binding of GFP-Cas1 and GFP-Cas2 was varied and dependent on the types of lipids.
313 Although we did not evaluate the disruption of these lipid membranes caused by GFP-
314 Cas1 and GFP-Cas2 using confocal microscopy, we consistently captured the large bright
315 clusters of GFP-Cas1 and GFP-Cas2 formed in the susceptible lipid membranes (see GFP
316 fluorescence in **Figures 4b1, b2, c1, d1, e2, f2, g2, h2**). This observation also implies that
317 the susceptible lipid components available in plants (PA, MGDG, DGDG, stigmasterol,
318 and sitosterol) recruited the binding and formation of Cas1 and Cas2 clusters in the lipid
319 membranes, as seen in our HS-AFM observation. Most likely, the formation and
320 expansion of the large Cas1 and Cas2 clusters in susceptible lipid membranes play crucial
321 roles in devastating lipid membranes.
322
323 **Cytotoxicity of Cas1 and Cas2 on rubber leaves**
324 To examine the cytotoxicity of Cas1 and Cas2 on rubber leaves at the cellular level,
325 this study addressed the second question of whether Cas1 and Cas2 could directly damage
326 and cause necrosis in rubber leaf tissues. Here, we tested the cytotoxicity of Cas1 and
327 Cas2 on freshly detached young rubber leaves of highly susceptible clones (*H.*
328 *brasiliensis* RRIV 1 and RRIV 4) and weakly susceptible clones (*H. brasiliensis* PB 255),
329 as reported previously (Hieu et al., 2020; Nguyen et al., 2014). In these experiments, 6 –
330 10 small spots on a rubber leaf's lower lamina side were slightly scraped on the cuticle
331 surface before applying 0.083 µg Cas1 or Cas2 to each spot. We evaluated the cytotoxicity
332 of Cas1 and Cas2 on rubber leaves by observing the color change and the size change in
333 the lesion spots. As seen in **Figure 5**, neither Cas1 nor Cas2 caused any noticeable damage
334 or color change in the infected spots of all rubber leaves after incubation for 24 h.
335 However, a green to brown color change was seen in some leaf lesion spots of susceptible
336 RRIV 1 and RRIV 4 rubber clones infected with Cas1 and Cas2 after incubation for 72 h.
337 The necrotic areas in the leaf lesion spots were largely expanded and seen after incubation
338 for 120 h (**Figures 5a1, a2, b1, b2**). In the case of the PB 255 rubber clone, necrosis in
339 the leaf lesion spots was developed and seen after treatment with Cas1 for 72 and 120 h
340 (**Figure 5c1**). However, necrosis in the leaf lesion spots developed very slowly and was
341 not clearly seen after treatment with Cas2 for 120 h (**Figure 5c2**). This observation
342 suggests that the cytotoxicity of Cas1 and Cas2 on the rubber leaves of a PB 255 clone
343 was different. Noticeably, some leaf spots infected with Cas1 changed from green to
344 brown and black colors (see black circles in **Figures 5a1, b1, c1**), while those infected
345 with Cas2 only changed from green to brown color (**Figures 5a2, b2**). The blackened
346 necrosis seen in lesion spots infected with Cas1 implies that Cas1 damaged leaf tissues

347 more severely than Cas2. Once the damage of Cas1 and Cas2 on leaf tissues began, leaf
348 tissue necrosis continuously developed and expanded in large areas. The cytotoxicity
349 assay on rubber leaves (RRIV 4 clone) with fungus *C. cassiicola* showed that the necrotic
350 leaf tissues surrounding filamentous fungi were produced and clearly seen at day5 and
351 day7 post inoculation (see brown halos, **Figure 5d**). This result suggest that Cas toxins
352 were made and secreted from fungus to damage the surrounding leaf tissues. Overall, we
353 demonstrated that both Cas1 and Cas2 could directly cause necrosis in the leaves of some
354 rubber clones. Our report also supports the previous finding of the cytotoxicity of Cas1
355 produced in *C. cassiicola* resulting in necrosis in rubber leaves (Ribeiro et al., 2019).
356 Indeed, the cytotoxicity of Cas2 on rubber leaves has never been reported before. Here,
357 we additionally report that Cas2 directly damaged and caused necrosis in rubber leaves.
358
359 **Dissecting cellular structures of rubber leaves using cryo-SEM**
360 This study addressed the third question of how Cas toxin could damage cellular and
361 tissue structures in rubber leaves. To answer this question, we used low voltage cryo-SEM
362 to anatomize the cellular and tissue structures in the leaf lesion spots developed in rubber
363 leaves of susceptible RRIV 4 clones after infection with Cas1 for ~120 h and compared
364 them to the structures in healthy control leaves. Indeed, ultralow-temperature and low-
365 voltage cryo-SEM has been proven to be a powerful technique for dissecting pristinely
366 fractured biological cells without conductive metal coatings (Osumi et al., 2006).
367 The lamina, cuticle, upper and lower epidermis, palisade mesophyll, and spongy
368 mesophyll in the healthy control leaves preserved their healthy cellular structures, which
369 were identified easily (**Figures 6A, B, C, D, and Figure 6-figure supplement 1**).
370 Additionally, intact cell walls and cytoplasmic membranes could be seen clearly in the
371 fractured leaf tissues (**Figures 6C, D, and Figure 6-figure supplement 1**). In contrast,
372 Cas1 strongly damaged the cellular and tissue structures in leaf lesion spots (**Figures 6E**
373 **and Figure 6-figure supplement 1**). The upper and lower epidermis, spongy, and
374 palisade parenchyma were devastated by Cas1. The cellular boundaries, such as cell walls
375 and cytoplasmic membranes, in the fractured leaf tissues were hardly distinguished.
376 Strikingly, large areas of cytoplasmic membranes in palisade mesophyll were found to be
377 severely devastated by Cas1. The binding of Cas1 clusters, pore formation, biofilm-like
378 formation, and expansion of Cas1 clusters at different degrees in the cytoplasmic
379 membranes were clearly observed (see white rectangles in **Figure 6E, Figure 6-figure**
380 **supplement 1**). Our results strongly suggest that cytoplasmic membranes were highly
381 vulnerable to the pathogenicity of Cas1. This mechanism may also be similarly applied
382 to understand the cytotoxicity of Cas2 on the leaves of susceptible rubber clones, although

383 it needs to be verified.
384
385 **Discussion**
386 **Cytoplasmic membrane vulnerability to Cas toxin plays a crucial role in HST**
387 **interactions**
388 Cytoplasmic membranes are essential in all living cells. In plant cells, life strongly
389 relies on the presence of a healthy functional cytoplasmic membrane enveloping the
390 cytosol, thereby forming a boundary between the internal and external cytosolic
391 environments. The cytoplasmic membrane plays pivotal roles in protecting cytosolic
392 contents, such as the chloroplast, Golgi apparatus, mitochondria, endoplasmic reticulum,
393 and nucleus, and furnishing a sophisticated lipid environment for various vital activities
394 across membranes, such as the transport activities of protein channels and transporters
395 (Assmann and Haubrick, 1996; Kang et al., 2011; Maure et al., 2008). Phospholipids (PC,
396 PA), glycerolipids (MGDG, DGDG), sterols (stigmasterol, sitosterol), and betaine lipids
397 (DGTS-d9, DGTS) are present in the cytoplasmic membranes of plant cells (Bae et al.,
398 2020; Dörmann and Benning, 2002; Dufourc, 2008a, 2008b; Hartmann, 1998;
399 Liengprayoon et al., 2011; Mackender and Leech, 1974; Murakami et al., 2018; Poincelot,
400 1976).[53]. The vulnerability of cytoplasmic membranes to Cas1 has been reported
401 previously (Barthe et al., 2007; de Lamotte et al., 2007). When observing the
402 ultrastructures of the necrotic leaf tissues caused by Cas1, they found that Cas1 severely
403 damaged the plasma membrane. Plasmolysis (e.g., membrane permeability) was modified.
404 The neutral deuterated (^{2}H)DPC membrane was weakly susceptible to Cas1, although
405 they could not rule out the interaction of Cas1 with other lipid classes (Barthe et al., 2007).
406 In this study, we showed that both Cas1 and Cas2 could directly damage and cause
407 necrosis in the leaves of some susceptible rubber clones. Our electron microscopic
408 analyses strongly suggest that cytoplasmic membranes were highly vulnerable to the
409 pathogenicity of Cas toxin (**Figures 6E and Figure 6-figure supplement 1**), supporting
410 the previous finding that Cas1 could damage cytoplasmic membranes (Barthe et al., 2007;
411 de Lamotte et al., 2007). We also explored here that the negative phospholipids (DPPA),
412 glycerolipids (MGDG, DGDG), and sterols (stigmasterol, sitosterol) available in
413 cytoplasmic membranes play key roles in the binding and disruption activity of Cas1 and
414 Cas2 to the cytoplasmic membrane. Neutral phospholipids (DPPC) and betaine lipids
415 (DGTS-d9, DGTS) are indeed weakly sensitive to the disruption activities of Cas1 and
416 Cas2. Our finding is crucial to understand the binding and disruption selectivity of Cas
417 toxin to different lipid compositions in cytoplasmic membranes.
418 Studying the HST interaction of Cas isoforms with lipid membranes is crucial to

419 understand the host-selective pathogen in CLF disease. Currently, the exact mechanism
420 remains unclear. In general, mycotoxins are categorized as host-specific or nonspecific
421 toxins. Some plant pathogenic fungi can synthesize mycotoxins as secondary metabolites
422 that act as virulence factors to develop severe fungal infections (Meena and Samal, 2019;
423 Petrov et al., 2018; Takaoka et al., 2014). Several important organelles inside plant cells,
424 such as the cytoplasmic membrane, chloroplasts, mitochondria, and endoplasmic
425 reticulum, have previously been suggested as target sites of selective AK toxins (Tsuge et
426 al., 2013). In particular, selective AK and fumonisin toxins were reported to damage or
427 modify cytoplasmic membranes in various ways (Park et al., 1976; Riley et al., 1996).
428 Here, we demonstrated that Cas1 and Cas2 directly damaged and caused necrosis in the
429 leaves of susceptible rubber clones (RRIV 1, RRIV 4, and PB 255). RRIV 1 and RRIV 4
430 clones were sensitive to both Cas1 and Cas2 (**Figures 5a1, a2, b1, b2**). Strikingly, a PB
431 255 clone was strongly resistant to Cas2 but susceptible to Cas1 (**Figures 5c1, c2**). These
432 results suggest that the cytotoxicity of the Cas1 and Cas2 isoforms varied in different
433 rubber clones, depending on the susceptibility of cytoplasmic membranes to the binding
434 and disruption of Cas toxin.
435
436 **Biofilm-like formation of Cas toxin and its physiological implication**
437 Strikingly, we also disclose that Cas toxin can form biofilm-like structures onto
438 specific lipid membranes composed of negative phospholipid (DPPA), glycerolipids
439 (MGDG, DGDG), and sterol (sitosterol) (**Figures 1b1, b2, c1, d1, d2, and 3A, B, and**
440 **Videos 3, 4, 5, 7, 8, 17, 18**). However, these biofilm-like structures are not formed on
441 lipid membranes composed of betaine lipids (DGTS-d9) (**Figure 3C, Video 19**). Our
442 realtime HS-AFM observation supports that the highly susceptible lipid membranes
443 containing negative phospholipid, glycerolipids, and sterol can recruit the binding of Cas1
444 and Cas2 onto their surfaces to form biofilm-like structures. The biofilms are either
445 covered on the membrane surface or partially incorporated onto the lipid membrane and
446 cause severe damage on membranes. Most likely, the biofilm-like formation of Cas toxin
447 also plays an important role in damaging cytoplasmic membranes, as seen in Cryo-SEM
448 images (**Figure 6E, Figure 6-figure supplement 1**).
449 Finally, we hypothesized the molecular mechanism of the host-selective toxic
450 interaction of Cas toxin with specific lipid membranes and its cytotoxicity on the
451 susceptible rubber leaves (**Figure 7**). The brown and black necrotic halos of leaf tissues
452 surrounding necrotrophic fungus *C. cassiicola* infected in rubber leaves are caused by the
453 selective Cas toxin secreted during the growth and invasion of fungus. The Cas toxin
454 binds to and strongly disrupts the specific and susceptible membrane lipids such as

455 negative phospholipids, glycerolipids, and sterols available in cytoplasmic membranes of
456 the specific plant cells. PA, MGDG, DGDG, and sitosterol lipids available in cytoplasmic
457 membranes may play an important role to recruit the binding and formation of biofilm-
458 like structures of Cas toxin onto cytoplasmic membranes. The selective binding and
459 disruption activities of Cas toxin on specific cytoplasmic membranes cause plasmolysis
460 and eventually cell death.
461
462 **Methods**
463 **Materials**
464 DNA oligonucleotides encoding cassiicolin (Cas) genes (Cas1 and Cas2) of
465 *Corynespora cassiicola* causing CLF disease in rubber trees (Déon et al., 2014, 2012b,
466 2012a) were purchased from IDT (Tokyo Japan). The PcoldGFP plasmid was a generous
467 gift from Prof. Taro Q.P. Uyeda (Waseda University, Japan). All necessary primers used
468 for PCR and cloning Cas1, Cas2, GFP-Cas1, and GFP-Cas2 were purchased from
469 Macrogen Japan (Tokyo, Japan). The oligonucleotides and amino acid sequences of Cas1
470 and Cas2 used in this study are summarized in **Table S5**. All synthetic lipids available in
471 plants were purchased from Avanti Polar Lipids (Alabama, USA). The structures and
472 physical properties of these lipids are clarified and summarized in **Figure S3**.
473
474 **Protein preparation**
475 The genes encoding Cas1 and Cas2 proteins were similarly inserted into the pColdI
476 vector at the *KpnI* and *XbaI* sites (Ngo et al., 2015). Similarly, the PcoldGFP vector
477 (generated two cloning sites by *BamHI* and *HindIII*) was employed to construct GFP-
478 Cas1 and GFP-Cas2 proteins. The successfully constructed plasmids for the expression
479 of Cas1, Cas2, GFP-Cas1, and GFP-Cas2 genes were confirmed by DNA oligonucleotide
480 sequences. All recombinant proteins containing a 6xHis-tag on the N-terminus (**Table S5**)
481 were designed for purification using a Ni-NTA resin column. For simplicity, we
482 consistently designated these recombinant proteins as Cas1, Cas2, GFP-Cas1, and GFP-
483 Cas2.
484 Cas1, Cas2, GFP-Cas1, and GFP-Cas2 were expressed in BL21 (DE3) *E. coli*
485 according to the manufacturer's instructions for PcoldI (Takara). Briefly, the transfected
486 *E. coli* cells were grown in LB broth containing 100 µg/ml ampicillin and 10 µg/ml
487 methyl 3-O(alpha-D-mannopyranosyl)-alpha-D-mannopyranoside (MDMDM) to an
488 OD600 of ~ 0.6. Then, the cell suspension was cooled to 15°C on ice. Protein expression
489 was induced by adding 1 mM IPTG. The cell suspension was continuously fermented in
490 a shaking incubator at 140 rpm and 15°C for 24 h. Then, the cells were harvested by low

491 centrifugation (4000 rpm, 10 min, 4°C). The cell pellet was gently washed twice with
492 cold 10 mM Tris-HCl buffer (pH 7.4). Next, the cell pellet was resuspended in lysis buffer
493 containing 50 mM Tris-HCl buffer (pH 8.0), 300 mM KCl, 5 mM EGTA, 20 mM
494 imidazole (pH 7.4), 1% (w/v) lauryl maltose neopentyl glycol (LMNG) (Anatrace), 10
495 mM β-mercaptoethanol, proteinase inhibitor cocktail (Sigma), and 1 mM PMSF. Cell
496 lysis was carried out overnight in a rotary incubator at 4°C. Next, the cells were finally
497 disrupted using a French press (repeated twice, ~140 MPa). After low centrifugation
498 (15,000 rpm, 15 min, 4°C), the crude protein solution was finally collected by
499 ultracentrifugation (40,000 rpm, 30 min, 4°C) and subsequently incubated with Ni-NTA
500 (GE healthcare) resin for 2 h at 4°C. The resin was recovered and transferred into a clean
501 plastic column for washing. The resin was washed carefully in cold wash buffer
502 containing 10 mM Tris-HCl (pH 7.4), 20 mM imidazole (pH 7.4), 1 M NaCl and 10 mM
503 β-mercaptoethanol until proteins in the washout solution were undetectable. Elution of
504 proteins was carried out with elution buffer containing 10 mM Tris-HCl (pH 7.4), 800
505 mM imidazole (pH 7.4) and 10 mM β-mercaptoethanol. The eluate was dialyzed against
506 dialysis buffer containing 10 mM Tris-HCl (pH 7.4), 50 mM KCl, 50% glycerol, and 10
507 mM β-mercaptoethanol using a dialysis membrane (MWCO 3300 Da) overnight at 4°C.
508 The dialysate was recovered and concentrated and finally subjected to low centrifugation
509 (15,000 rpm, 10 min, 4°C) to remove any protein aggregates. Protein concentration was
510 measured by the Bradford method or UV absorption (Cas1: ε_{280} = 8855 M^{-1}. cm^{-1} or A_{280}
511 = 0.984 (1 mg/ml), 9003.27 Da; Cas2: ε_{280} = 8855 M^{-1}. cm^{-1} or A_{280} = 0.981 (1 mg/ml),
512 9025.28 Da; GFP-Cas1: ε_{280} = 29380 M^{-1}. cm^{-1} or A_{280} = 0.830 (1 mg/ml), 35400.95 KDa;
513 GFP-Cas2: ε_{280} = 29380 M^{-1}. cm^{-1} or A_{280} = 0.815 (1 mg/ml), 35422.07 KDa). Small
514 aliquots of proteins were snap-frozen in liquid nitrogen and stored at -80°C. The activities
515 of target proteins were characterized by common biochemical assays, mass spectrometry,
516 HS-AFM, confocal microscopy, cryo-SEM, and cytotoxicity assays on rubber leaves.
517
518 **Giant liposome vesicles**
519 We made giant liposome vesicles (GVs) from different lipids available in plants for
520 imaging the binding of GFP-Cas1 and GFP-Cas2 to different lipid membranes using
521 confocal microscopy. The electroformation methods for making GVs have been well
522 established in several previous studies (Angelova and Dimitrov, 2007, 1986; Dimitrov
523 and Angelova, 1988). The lipid compositions are described in **Table S3** and clarified in
524 **Figure S3**. Briefly, the lipid mixtures dissolved in chloroform were stored at -20°C. The
525 mixtures were warmed at room temperature for 10 min. A 20 μl lipid mixture was
526 thoroughly spread on indium tin oxide (ITO)-coated glass slides (Nanion, Germany). The

527 dried thin film was formed by the complete evaporation of chloroform at room
528 temperature for approximately 10 min. To make GVs on the ITO-coated glass slide, we
529 used a Vesicle Prep Pro (Nanion, Germany). An O-ring with a diameter of 16 mm was
530 used to make a chamber furnishing the dried thin film inside. A 250 µl filter sterile
531 electroformation buffer containing 1 M D-sorbitol, 1 mM EGTA, and 2 mM HEPES-
532 NaOH (pH 7.4) was applied into a chamber sandwiched between two conductive sides of
533 the ITO-coated glass slides. The protocol for making GVs was set up as follows: Initial
534 (0 V, 5 Hz, 50°C, 5 min); Start (3 V, 10 Hz, 50°C, 10 min); Main (3 V, 10 Hz, 50°C, 60
535 min); Fall (0 V, 10 Hz, 50°C, 5 min); End (0 V, 10 Hz, 20°C). The formed GVs were
536 gently collected and stably stored at 4°C for approximately 1 – 2 weeks.
537
538 **Confocal microscopy**
539 The FluoroDish cell culture dishes (FD35-100, WPI) were cleaned by dipping in 3
540 M KOH solution for 1 h, subsequently washed in Milli-Q water approximately 10 times,
541 dried at 60°C for 1 h or more, and stored at room temperature before use. GV solution
542 (~0.8 mM lipid) was diluted in imaging buffer containing 5 mM HEPES-NaOH (pH 7.4),
543 5 mM NaCl, 0.05 mM EDTA, and 1 M D-sorbitol to a final lipid concentration of ~0.2
544 mM. To assay the binding of Cas1 or Cas2 to different lipid membranes, we gently mixed
545 9.5 µM GFP-Cas1 or GFP-Cas2 with 100 µl of diluted GV solution, incubated the mixture
546 at room temperature for 5 min, and subsequently introduced the mixture into a cleaned
547 FluoroDish. In most cases, we could image the GVs weakly absorbing onto the glass
548 surface by gravity force. Only in the case of negatively charged DPPC/DPPA GVs did we
549 further added 300 mM NaCl and 10 mM $MgCl_2$ into the imaging buffer for better
550 absorption of these GVs onto the glass surface.
551 Confocal imaging experiments were performed in a STED confocal microscopy
552 (Abberior Instruments, Germany). We used a 100x oil-immersed objective lens
553 (NA=1.46). Images were taken using Imspector software. Two channel images were
554 acquired one by one for each pixel at 50 x 50 x50 nm resolution per xyz pixel.
555 The confocal imaging conditions were set up as follows: SiR channel (Ex: 652 nm) for
556 rhodamine, EGFP channel (Ex: 489 nm) for GFP, 15% laser power source used for both
557 channels. The images were analyzed using Fiji-ImageJ (NIH, USA). Initially, we
558 corrected the background for both channels. After a Gaussian-blur filter (sigma radius
559 = 2.0) was applied, the images were converted to binary images with a minimum
560 threshold set value of 12 for measuring the pixel areas in each channel. The rhodamine
561 area where Cas is not bound was calculated by subtracting the GFP channel from the
562 rhodamine channel. Then, the relative fluorescence area was calculated for a quantitative

comparison of the binding area of GFP-Cas1 and GFP-Cas2 to different GVs.

Mass spectrometry

The target Cas1 protein band was excised from the electrophoresis gel and subjected to in-gel digestion (Hellman et al., 1995). The peptide fractions were analyzed by a solariX (Bruker Daltonics, Billerica, USA), as previously described (Kawakita et al., 2016).

High-speed atomic force microscopy

We used a laboratory-built high-speed atomic force microscope (HS-AFM) as described previously (Ando et al., 2008; Ngo et al., 2015; Uchihashi et al., 2012). HS-AFM imaging was carried out in solution using tapping mode with small cantilevers (BL-AC10DS-A2, Olympus, Tokyo, Japan) whose spring constant, resonant frequency in water, and quality factor in water were ~0.1 N/m, ~500 kHz, and ~1.5, respectively. Our lab-made ferrocene tip on an original tip-less cantilever was grown through electron beam deposition (EBD) using scanning electron microscopy (ZEISS Supra 40 VP/Gemini column, Zeiss, Germany). Typically, the EBD tip was grown under vacuum (1 – 5 x 10^{-6} Torr), aperture size (10 μm), and EHT voltage (20 kV) for 30 s. The EBD ferrocene tip was further sharpened using a radio frequency plasma etcher (Tergeo Plasma Cleaner, Pie Scientific, CA, USA) under an argon gas atmosphere (typically at 180 mTorr and 20 W for 30 s). During HS-AFM imaging, the free-oscillation peak-to-peak amplitude of the cantilever (A_0) was set to ~1.6 – 1.8 nm, and the feedback amplitude set-point was set at ~0.9A_0.

Real-time imaging of disruption of lipid membranes caused by Cas1 and Cas2

We prepared small unilamellar vesicles (SUVs) or liposomes by the thin-film hydration method and mica-supported lipid bilayer as described previously (Ngo et al., 2015). In this study, DPPC, DPPC/DPPA (80/20 wt%), DPPC/MGDG (80/20 wt%), DPPC/DGDG (60/40 wt%), DPPC/stigmasterol (80/20 wt%), DPPC/sitosterol (80/20 wt%), DPPC/DGTS-d9 (80/20 wt%), and DPPC/DGTS (80/20 wt%) liposomes were made. Typically, liposomes were made in Milli-Q water at 1 mg/ml and stored at −20°C. To form a lipid bilayer on mica, liposomes were diluted in 10 mM $MgCl_2$ to 0.1 mg/ml and sonicated with a bath sonicator at room temperature (AUC-06 L, AS ONE, Osaka, Japan) for 1 min. Then, 2 μl of the sonicated liposomes was deposited on the surface of freshly cleaved mica (2 mm in diameter), which had been glued onto a glass stage

599 beforehand, and incubated for approximately 2 h at room temperature (24 – 26°C) in a
600 humid sealed container to avoid surface drying.
601 Real-time imaging of the binding and disruption activities of Cas1 and Cas2 to lipid
602 membranes formed on mica was carried out in C-buffer containing 10 mM HEPES-NaOH
603 (pH 7.4), 0.1 mM EDTA, and 100 mM NaCl at room temperature by using HS-AFM. In
604 all HS-AFM experiments excepted noted, we consistently used 0.95 μM Cas1 or Cas2 as
605 a final concentration to examine the susceptibility of different lipid membrane
606 compositions to Cas1 and Cas2. The sample volume in the HS-AFM imaging experiment
607 was ~70 μl.
608
609 **Cytotoxicity on rubber leaves caused by Cas1 and Cas2**
610 Young and healthy leaves of rubber trees (*H. brasiliensis* RRIV 4, RRIV 1, and PB
611 255 clones) grown in southern Vietnam were freshly collected in the early morning. It
612 usually took 4 – 5 h before a cytotoxicity test. The leaves were carefully disinfected with
613 60% ethanol and sterilized Milli-Q water. Three rubber leaves were placed on a plastic
614 net under one experimental condition and separately incubated inside a plastic box (40
615 cm x 40 cm x 5 cm). The moisture was maintained by laying down wet Whatman filter
616 paper under a plastic net, avoiding direct contact with leaves. To test the cytotoxicity of
617 Cas1 and Cas2 on rubber leaves, 6 to 10 small spots on the lower lamina sides of leaves
618 were chosen and slightly scraped on the cuticle wax layer with a small pipette tip. Next,
619 10 μl of 0.0083 μg/μl (~ 0.083 μg) Cas1 or Cas2 was applied to each spot. The molar
620 concentration of Cas1 and Cas2 infected in each spot was kept almost the same as that
621 used for HS-AFM observation, although the final sample volume used in HS-AFM
622 observation was ~ 7 times higher. The control experiments were performed similarly by
623 applying 10 μl of sterilized Milli-Q water to each spot. The control and infected leaf
624 samples were separately incubated and maintained under the same humidity (~80 – 90%)
625 and temperature (~26 – 28°C) in the dark. For sample analyses, leaves in each moist
626 plastic box were carefully photographed after 24, 72, and 120 h of infection by using a
627 conventional digital camera. Each experimental condition was repeated 2 – 3 times. The
628 leaf lesion spots caused by Cas1 and Cas2 on different rubber clones were compared by
629 observing color changes and lesion size and dissecting the cellular structures by cryo-
630 SEM.
631 Pathogenicity test on rubber leaves with *C. cassiicola*: Healthy rubber leaves (RRIV
632 4 clone) were washed with 0.2% sodium benzoate for 30 seconds, then followed by
633 rinsing three times with sterile distilled water. After draining the leaves with sterile paper,
634 rubber leaves were put up side down on the wire mesh in plastic containers in order to

separate the leaves and moisture absorbent paper. The infection on rubber detached leaves was conducted by dropping 10 µl of *Corynespora cassiicola* conidial solution with the concentration of $2x10^3$ spores/ml at 8 points per leaf using micro pipette. Next, the plastic containers were placed in a room at 25°C and humidity (80 – 90%) under 12 hours of fluorescent light per day within six days. The pathogenicity of *C. cassiicola* was evaluated and recorded based on the modified method by Nghia et al., 2008.

Cryo-SEM imaging

We selected the healthy (control, + water, 120 h) and infected (+ Cas1, 120 h) leaves of one rubber clone (RRIV 4) to anatomize the leaf tissues and cellular structures. To make the Cryo-SEM samples, healthy and lesion-containing areas surrounding the initially scraped spots were chosen. The ultrastructures of leaf tissues were analyzed by low voltage cryo-scanning electron microscopy (Cryo-SEM), a powerful technique for imaging pristinely fractured biological cells without conductive metal coating (Osumi et al., 2006). Leaf samples were punched out with a 3 mm diameter circular blade and plunged into liquid ethane at 90 K. Cryo-SEM images were obtained from a Helios G4 CX (Thermo Fisher Scientific, USA) with a PP3010 Cryo-SEM transfer system (Quorum Technologies, UK). Frozen leaf samples were clamped perpendicular at the top and the center of a metal cylinder on the transfer shuttle and fractured inside the vacuum chamber to face the freshly fractured depth profile just on the top of the cylinder without conductive metal coating. No ice contamination growth was visible during the fracture of samples under high vacuum conditions below a pressure of 5.0×10^{-5} Pa. The sample stage temperature was kept at 93 K. A 1 kV electron beam of the landing energy with a stage bias voltage of 2 kV was used substantially in low voltage cryo-SEM imaging of the fractured sample surfaces embedded in a cylindrical shape holder. Notably, only when the lower lamina side of rubber leaves was imaged we coated the leaf surface with platinum in the vacuum chamber before imaging.

Analyses of HS-AFM images

HS-AFM images were viewed, analyzed, and exported by using the laboratory built software Kodec4.4.7.39. Kodec4.4.7.39 software was coded in Visual C# (Visual Studio 2010, Microsoft, USA), and source code 1 is openly available (Ngo et al., 2015). All filters and subroutines for image analyses used in the present study were included in the software. We confirmed the compatibility between the software and computers operated with Windows 8 or 10. This software should be cited as Sakashita M, M Imai, N Kodera, D Maruyama, H Watanabe, Y Moriguchi, and T Ando. 2013. Kodec4.4.7.39. Briefly,

AFM images were flattened and filtered (Gaussian blur, Sigma radius: 1 nm) to increase the S/N ratio. AFM images were converted and extracted to BMP format images. The image sequences were converted to a Video format (AVI) using Fiji-ImageJ software (NIH, USA).

Artworks

All illustrative graphics used in this study were done by using Biorender, Adobe Illustrator 2021 (Adobe, USA). Data figures were made by Origin Pro 2016 graphic software (OriginLab, USA) and Igor Pro graphic software (Wavematrics Inc., USA).

Statistics

All data (mean ± SD) were statistically processed using an Origin Pro 2016 graphic software (OriginLab, USA). The differences were statistically tested using two-independent populations *t-test*.

Acknowledgements

This work was partly supported by FY2018 and FY2019 Bio-SPMs Collaborative Research of WPI Nano Life Science Institute (WPI-NanoLSI), Kanazawa University, Japan to NBQ and KXN, and partly funded from Ho Chi Minh City Open University (No. E2019.05.1), Vietnam to NNBC; Grants-in-aid from the Ministry of Education, Culture, Sports, Science and Technology, Japan to KXN (No. 19K06581). We deeply thank Prof. Taro Q.P. Uyeda (Waseda University) for his generous gift of a plasmid. We thank Dr. Thien Quang Huynh (Kanazawa University, Vietnam Academy of Science and Technology) for sample preparation and data analysis.

Author contributions

KXN and NBQ designed concepts. KXN designed and constructed plasmids, and KXN, PDNN, TOM expressed, purified, and analyzed proteins. NBQ, PDNN, NNBC, NPV, and NAN performed the cytotoxicity test. KXN and PDNN performed HS-AFM imaging. HF, KXN, and NBQ performed cryo-SEM observation and analyzed data. TS, MM, and KXN performed mass spectrometry and analyzed data. KXN, TI, and TF performed confocal microscopy. KXN, PDNN, NK, TA, HK, and NBQ analyzed HS-AFM data. KXN, NBQ, and TA wrote the manuscript.

Competing interest statement

The authors declare no competing interests.

Nomenclature

DPPC: 1,2-dipalmitoyl-sn-glycero-3-phosphocholine

DPPA: 1,2-dipalmitoyl-sn-glycero-3-phosphate

MGDG: Monogalactosyldiacylglycerol

DGDG: Digalactosyldiacylglycerol

DGTS-d9: 1,2-dipalmitoyl-sn-glycero-3-O-4'-[N,N,N-trimethyl(d9)]-betaine

DGTS: 1,2-dipalmitoyl-sn-glycero-3-O-4'-(N,N,N-trimethyl)-betaine

GVs: giant liposome vesicles

Cas: cassiicolin

CLF: corynespora leaf fall

CCP: pathogenic *C. cassiicola* isolates in rubber trees originally from the Philippines

HS-AFM: High-speed atomic force microscopy

Cryo-SEM: cryo-scanning electron microscopy

MALDI FT-ICR: matrix-assisted laser desorption/ionization Fourier-transform ion cyclotron resonance

IPTG: Isopropyl β-D-1-thiogalactopyranoside

PMSF: Phenylmethylsulfonyl fluoride

MWCO: Molecular weight cutoff

RRIV: Rubber research institute of Vietnam

PB: Prang Besar (a name of a rubber research center in Malaysia)

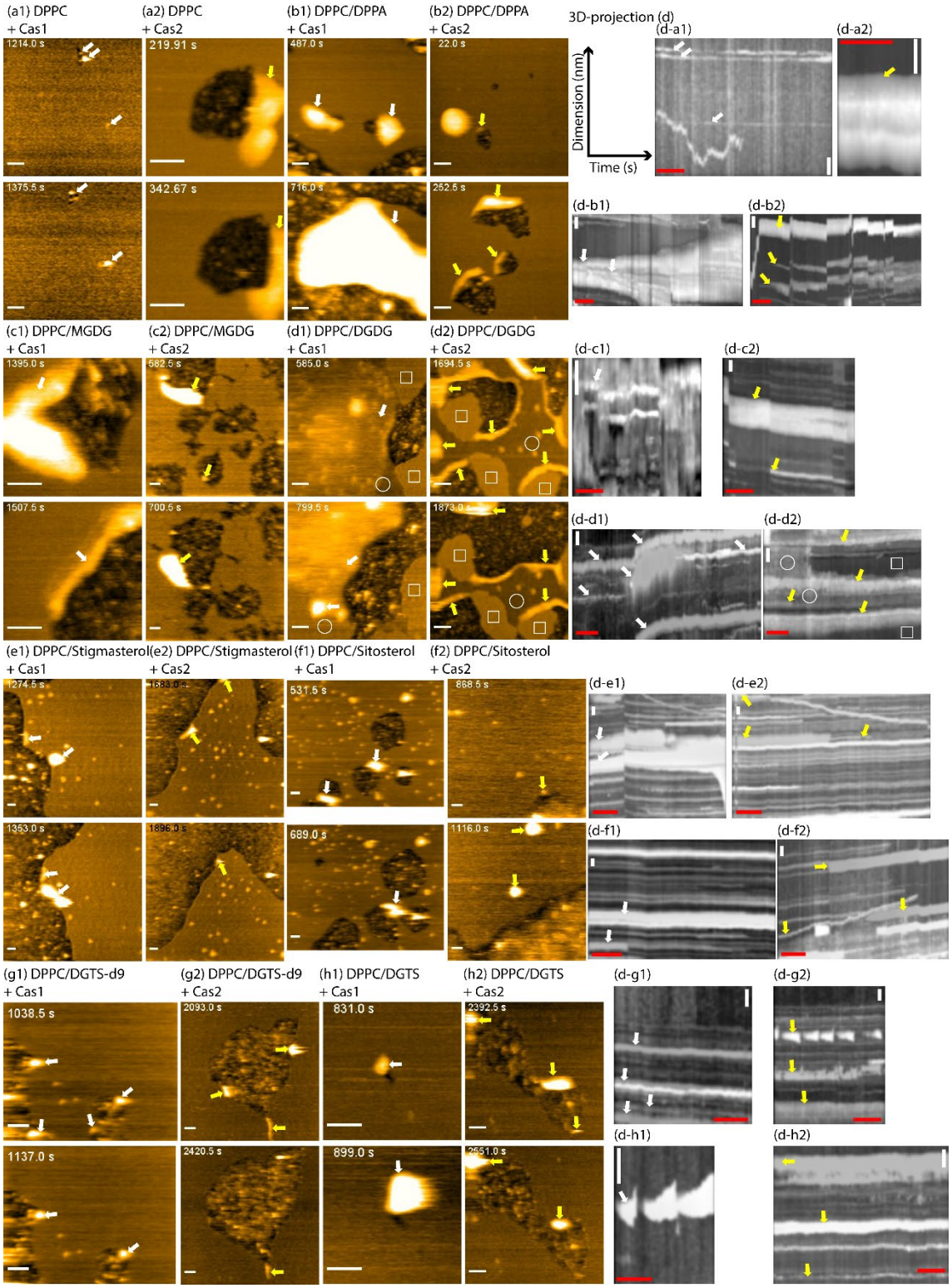

Figure 1. HS-AFM imaging of disruption processes of different membrane lipids available in plants induced by Cas1 and Cas2. **d-a1 – d-h2**: 3D projection analyses corresponding to a1 – h2 and Videos 1 – 16, respectively, to track the dynamics of Cas

clusters formed and incorporated onto lipid membranes. Briefly, lipid bilayers consisting of different lipid compositions were formed on mica by rupturing liposomes. Then, 0.95 μM Cas1 or Cas2 was added, and HS-AFM imaging was carried out in C-buffer using a BL-AC10DS-A2 cantilever deposited with a small lab-made tip. White and yellow arrows: Cas1 and Cas2 clusters, respectively, incorporated into the lipid bilayer. Rectangles and circles in d1 and d2 denote DPPC and DGDG domains, respectively. Imaging rate: 2 fps. The time label in still images denotes a time point after the addition of Cas1 or Cas2. In kymographs, white bars: 50 nm, red bars: 25 s. **Related to Videos 1 – 16, and Table 1**.

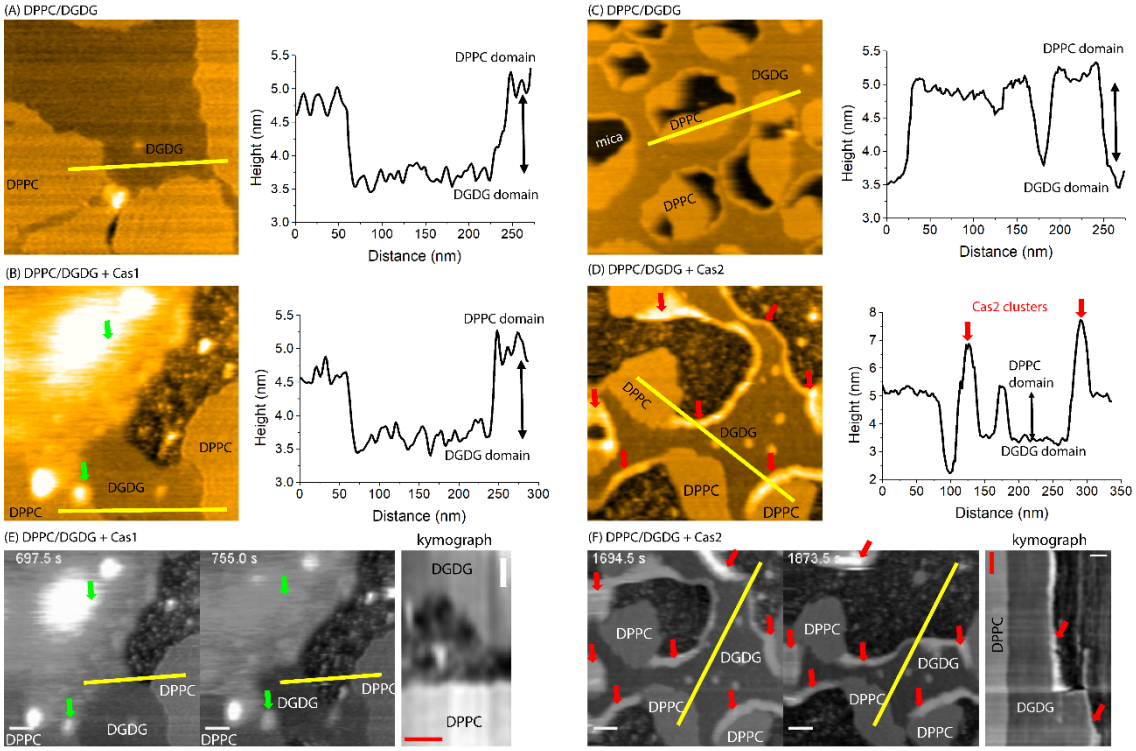

Figure 2. HS-AFM topographic image analyses. (A, B) HS-AFM images and topographic profiles of the DPPC/DGDG lipid bilayer formed on mica in the absence and presence of Cas1. (C, D) HS-AFM images and topographic profiles of the DPPC/DGDG lipid bilayer formed on mica in the absence and presence of Cas2. (E, F) Kymographs demonstrate the selective disruption activities of Cas1 and Cas2, respectively, on DPPC and DGDG membrane domains. DPPC, DGDG, and Cas clusters were distinguished by height differences. The time label in still images denotes a time point after the addition of Cas1 or Cas2. Green arrows: Cas1 clusters, red arrows: Cas2 clusters. In kymographs, white bars: 50 nm, red bars: 25 s. **<u>Related to Figures 1d1 – d2 and Videos 7 – 8.</u>**

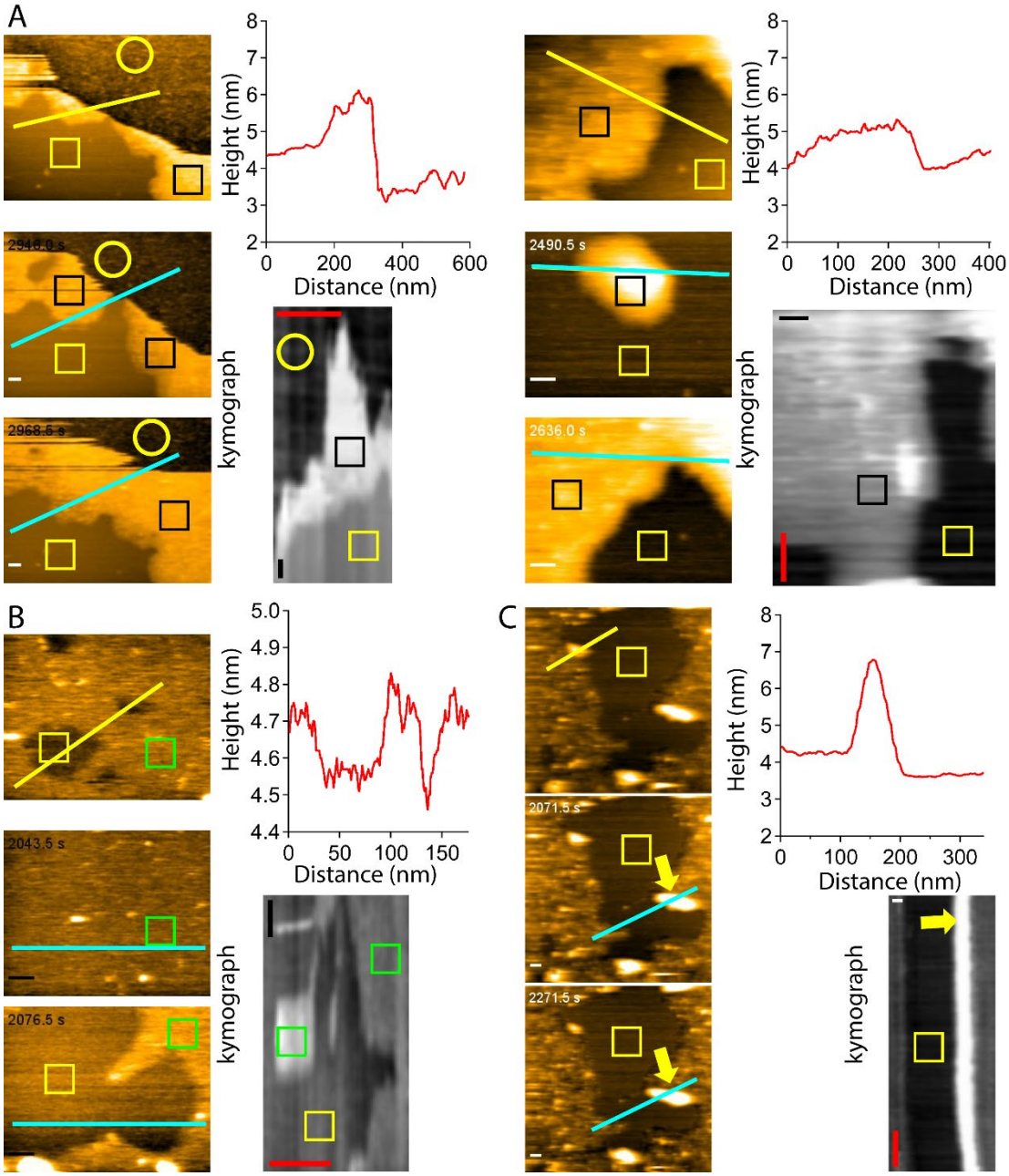

Figure 3. Biofilm-like structures of the Cas1/Cas2 mixture formed on the specific lipid membranes. (A) Biofilm-like structures of the Cas1/Cas2 mixtures formed on DPPC/sitosterol (80/20 wt%) membranes; (B) Biofilm-like structures of Cas2 formed on DPPC/sitosterol (80/20 wt%) membranes; (C) No formation of the biofilm-like structures of the Cas1/Cas2 mixtures on DGTS-d9 (80/20 wt%) membranes. The final concentration of Cas1 and Cas2 were 4.75 μM. The topographic profiles of biofilm-like structures are shown (yellow and red lines). The kymographs demonstrate the dynamics of biofilm-like formation as a function of time (cyan lines). The time label in still images denotes a time point after the addition of Cas1 and Cas2. Yellow arrows denote Cas clusters formed on

DPPC/DGTS-d9 membranes. Black, yellow, and green rectangles denote biofilm-like areas (Cas1/Cas2 mixtures), lipid membranes, and biofilm-like areas (Cas2), respectively. Yellow circles denote the lipid/Cas1/Cas2 mixtures left on mica after the disruption process. In kymographs, white and black bars: 50 nm, red bars: 25 s. **Related to Videos 17, 18, and 19**.

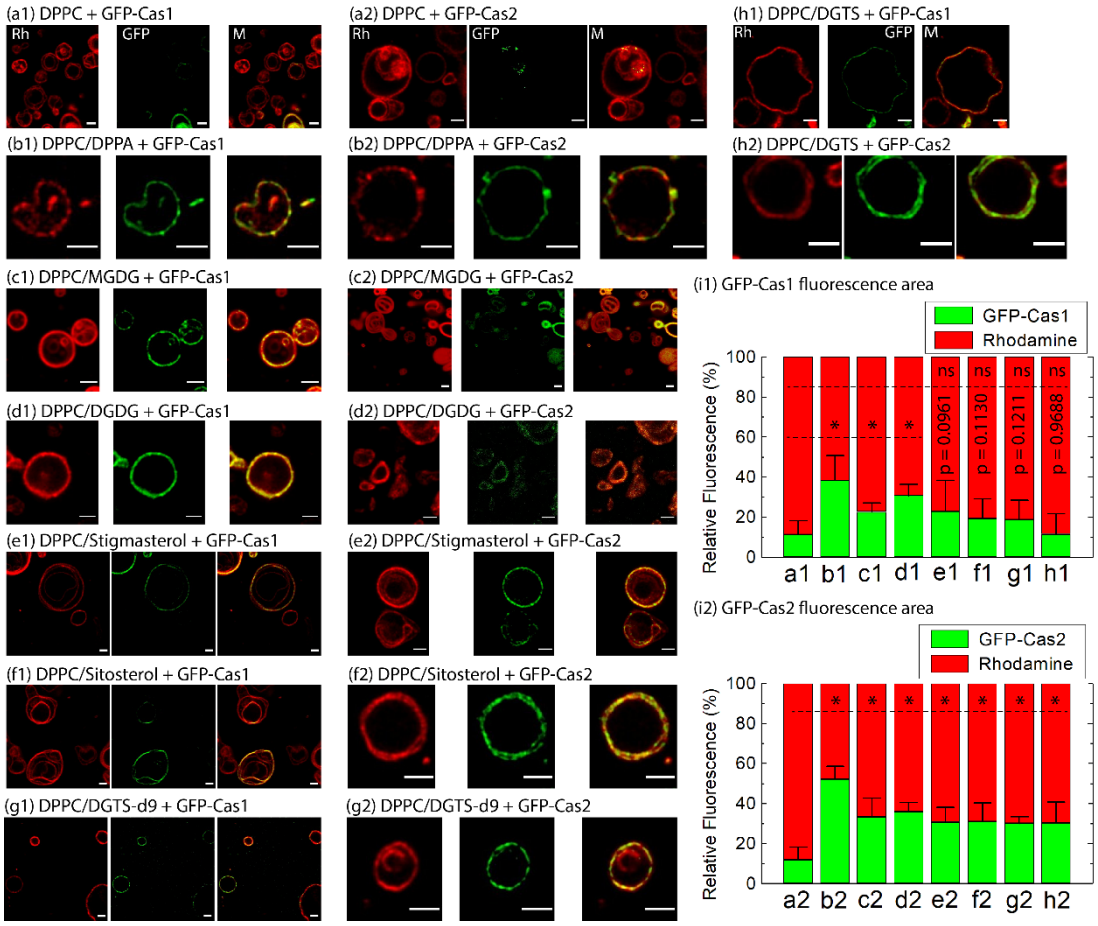

Figure 4. Confocal microscopic imaging to quantify the binding of GFP-Cas1 and GFP-Cas2 to GVs made of different lipids available in plants. The final concentration of GFP-Cas1 and GFP-Cas2 was 9.5 µM. From left to right (a1 – h1, a2 – h2), Rh denotes rhodamine-PE, GFP denotes GFP-Cas1 or GFP-Cas2, M: merged. (i1 and i2) Quantification of relative fluorescence areas of GFP-Cas1 and GFP-Cas2 on various GVs described from a-h. The values are mean ± SD. GFP fluorescence areas on DPPC GVs were used as the controls for comparison with those on other GVs. Asterisks (*) show a significant difference ($p \leq 0.05$, two-independent populations *t-test*). *p*-values are shown when the difference is not significant (ns) at the indicated level ($p \leq 0.05$). Number of values in each population: 6 – 11. Bars: 5 µm. **Related to Tables 1, 2**.

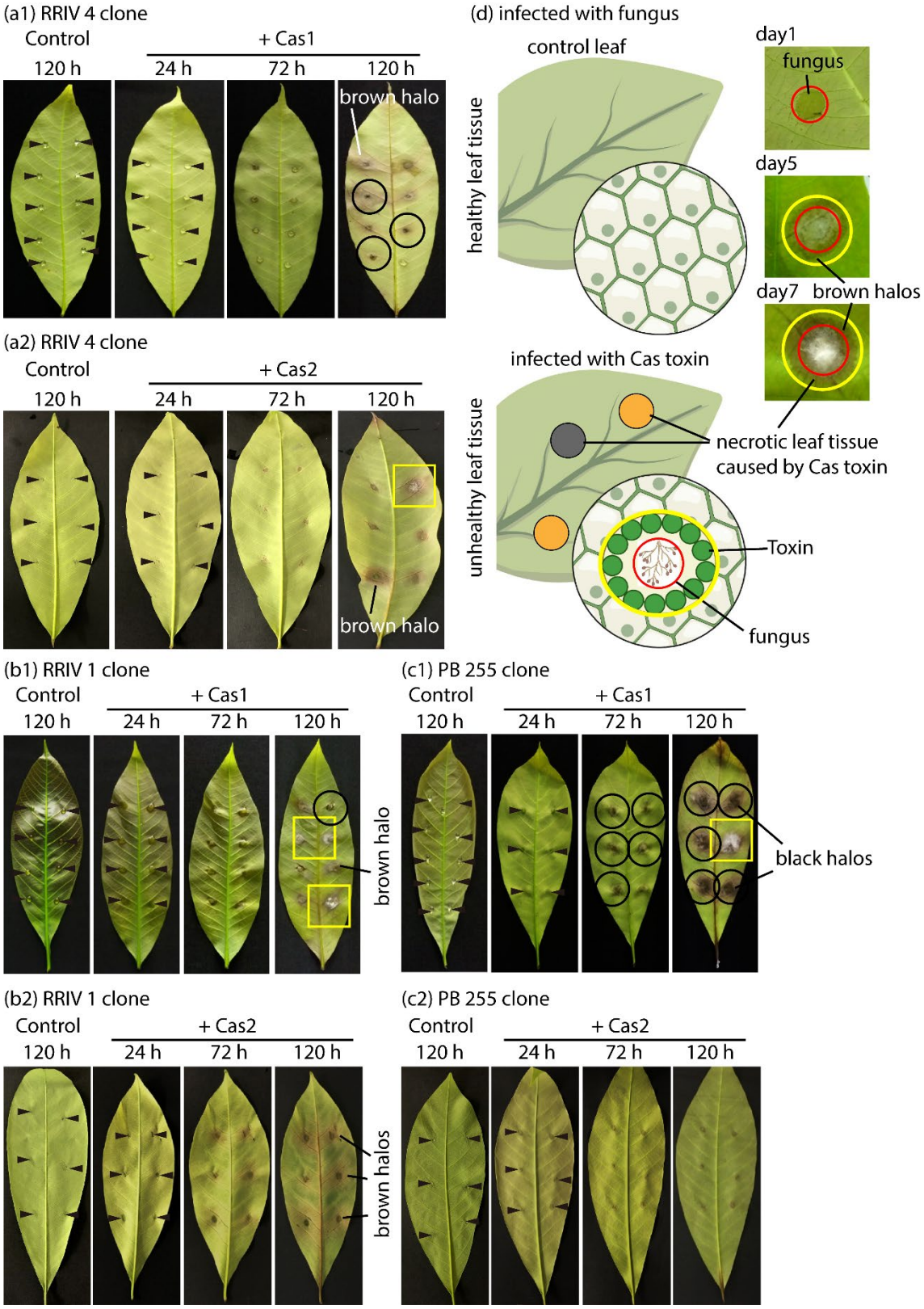

Figure 5. Cytotoxicity of rubber leaves of RRIV 4, RRIV 1, and PB 255 clones caused by Cas1 and Cas2. Six to ten small spots on the lower lamina sides of the healthy rubber

leaves were slightly scraped before cytotoxicity tests. (a1 – c2): Control: Ten microliters of sterilized water were applied to each spot. Infected leaves: Ten microliters of 0.0083 µg/µl (~0.083 µg) Cas1 or Cas2 were applied to each spot. Control and infected leaves were separately incubated under the same humidity (~80 – 90%) and temperature (26 – 28°C) and photographed after incubation at 24, 72, and 120 h by a conventional digital camera. (d) Rubber leaves (RRIV 4 clone) were infected with 10 µl conidial solution of fungus *C. cassiicola* ($2x10^3$ spores/ml) and inoculated at 25°C and humidity (~80 – 90%). Arrowheads: Initial positions of the infected spots. Black circles: blackened lesion spots: Rectangles: possible contamination of fungus. In (d), red circles: *C. cassiicola* growing areas; space between red and yellow circles: brown halos of necrotic leaf tissues caused by Cas toxin secreted from fungus. **Related to Figure 6 and Figure 6-figure supplement 1**.

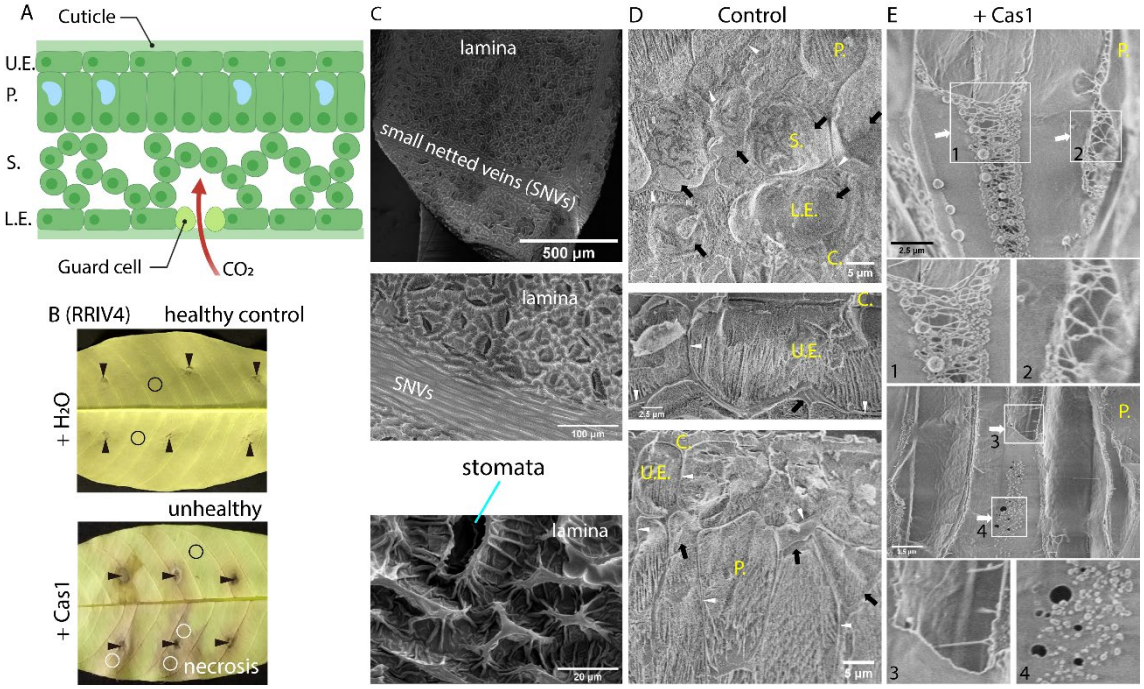

Figure 6. Cryo-SEM images of cellular and tissue structures of healthy controls and lesion spots in rubber leaves (RRIV 4 clone) caused by Cas1. (**A**) An illustration of leaf tissue anatomy; (**B**) Lower lamina side of the healthy control and infected rubber leaves (+ 0.083 µg Cas1) after incubation for ~ 120 h. The small areas of the healthy control (black circles) and lesion spots (white circles) in rubber leaves shown in B were punched out and plunged into liquid ethane, and cellular and tissue structures were dissected. Black arrowheads: initially infected spots. (**C**) Lower lamina side of rubber leaves. (**D**, **E**) Cellular and tissue structures of the healthy control and lesion spots, respectively. Black and white arrows denote the healthy and damaged cytoplasmic membranes, respectively. White arrowheads: the healthy cell wall. C: cuticle, U.E.: upper epidermis, L.E.: lower epidermis, P.: palisade mesophyll, S.: spongy mesophyll. White rectangles denote biofilm-like structures of Cas1 formed on cytoplasmic membrane. **Related to Figure 5 and Figure 6-figure supplement 1**.

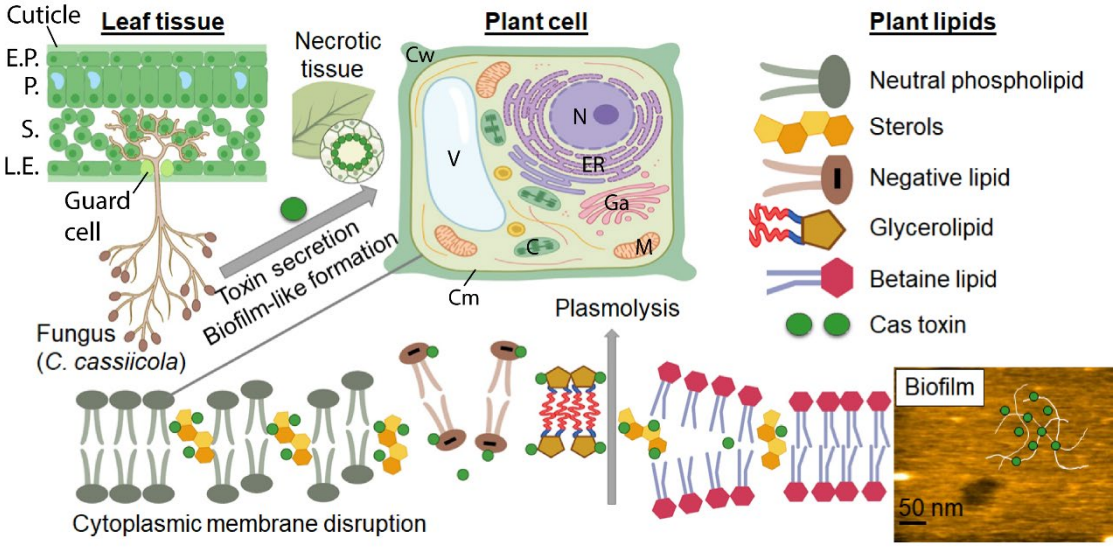

Figure 7. Hypothesis of the host-selective toxic interaction of Cas toxin with specific lipid membranes and its cytotoxicity arise from the formation of biofilm-like structures and disruption activities onto specific cytoplasmic membranes composed of susceptible plant lipids (i.e., negative phospholipids (PA), glycerolipids (MGDG, DGDG), and sterols (stigmasterol, sitosterol)). Cas toxin (Cas1, Cas2), Cm: cytoplasmic membrane, Cw: cell wall, N: nucleus, ER: endoplasmic reticulum, Ga: Golgi apparatus, C: chloroplast, M: mitochondria, V: vacuole, U.E.: upper epidermis, L.E.: lower epidermis, P.: palisade mesophyll, S.: spongy mesophyll.

938 **Table 1**. Classification of the susceptibility of different lipids available in plant
939 cytoplasmic membranes to Cas1 and Cas2. Here, we compared the binding and disruption
940 activities of Cas1 and Cas2 onto the lipid membranes acquired in HS-AFM and confocal
941 microscopic analyses. The binding and disruption activities of Cas1 and Cas2 to the
942 neutral DPPC lipid membranes were used as the basal indicator for a semi-quantitative
943 comparison. ++: strong; +: weak; B: Binding; D: Disruption. **Related to Figures 1, 2, 3,**
944 **and 4, and Videos 1 – 16**.

	DPPC	DPPC/ DPPA	DPPC/ MGDG	DPPC/ DGDG	DPPC/ Stigmasterol	DPPC/ Sitosterol	DPPC/ DGTS-d9	DPPC/ DGTS
+ Cas1	B (+)	B (++)	B (++)	B (++)	B (+)	B (+)	B (+)	B (+)
	D (+)	D (++)	D (++)	D (++)	D (++)	D (++)	D (+)	D (+)
+ Cas2	B (+)	B (++)	B (++)	B (++)	B (++)	B (++)	B (++)	B (++)
	D (+)	D (++)	D (++)	D (++)	D (++)	D (++)	D (+)	D (+)

945
946
947
948
949
950
951
952
953
954
955
956
957
958
959
960
961
962
963
964
965
966

967 **Table 2**. Quantification of relative fluorescence areas of GFP-Cas1 and GFP-Cas2 on
968 different composite GVs. The values are mean ± SD. The two-independent populations *t-*
969 *test* was used to examine the significant differences, and *p*-values and number of values
970 (N) are shown in parentheses. GFP fluorescence areas on DPPC GVs were used as the
971 controls for comparison with those on other GVs. **Related to Figure 4**.

GVs Samples	**Relative fluorescence areas of GFP-Cas1 (mean ± SD) %** (*p* value, N)	**Relative fluorescence areas of GFP-Cas2 (mean ± SD) %** (*p* value, N)
a1,a2 (DPPC)	11.2 ± 6.9 (1.0000, 8)	11.8 ± 6.4 (1.0000, 7)
b1.b2 (PPPC/DPPA)	38.1 ± 12.7 (0.0002, 8)	52.2 ± 6.4 (0.0000001, 7)
c1,c2 (DPPC/MGDG)	22.5 ± 4.6 (0.0048, 7)	33.2 ± 9.5 (0.0006368, 7)
d1,d2 (DPPC/DGDG)	30.7 ± 5.7 (0.00003, 9)	35.9 ± 4.6 (0.0000004, 10)
e1,e2 (DPPC/stigmasterol)	22.7 ± 15.7 (0.0961, 8)	30.6 ± 7.5 (0.0002098, 9)
f1,f2 (DPPC/sitosterol)	19.2 ± 9.9 (0.1130, 8)	30.9 ± 9.3 (0.0004778, 10)
g1,g2 (DPPC/DGTS-d9)	18.6 ± 9.7 (0.1211, 8)	30.0 ± 3.4 (0.0001303, 6)
h1,h2 (DPPC/DGTS)	11.4 ± 10.3 (0.9688, 7)	30.3 ± 10.5 (0.0011800, 11)

972
973
974
975
976
977
978
979
980
981
982

983 **Figure supplements**

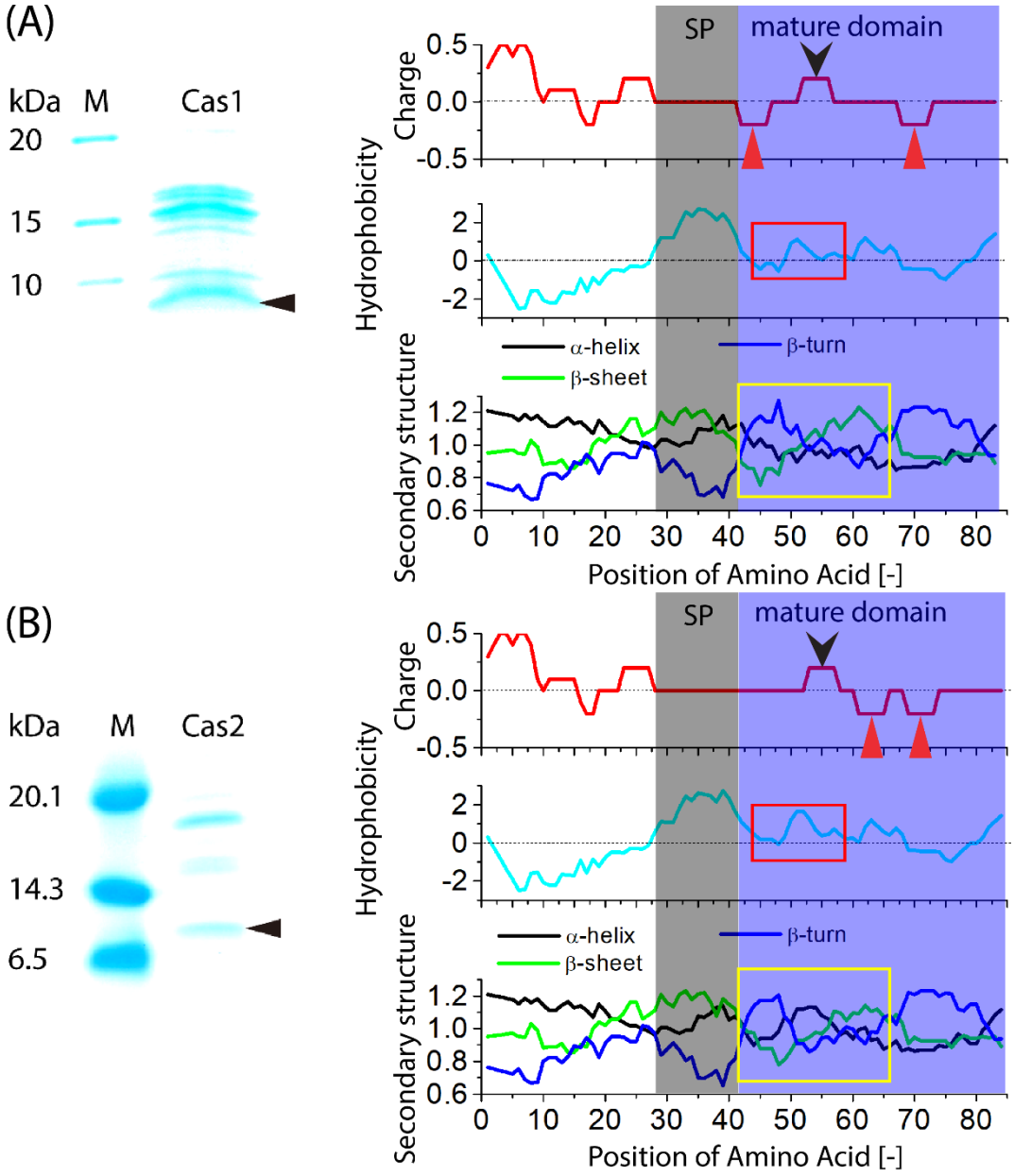

984

985 **Figure 1-figure supplement 1**. Purification of Cas1 and Cas2 from *E. coli*. (**A**) SDS-
986 PAGE gel images of Cas1 and Cas2 stained with Coomassie Brilliant Blue R-250 (CBB)
987 (**B**) Computing charge (http://www.bioinformatics.nl/cgi-bin/emboss/charge),
988 hydrophobicity, and secondary structure (alpha-helix, beta-sheet, and beta-turn) scales
989 based on the profiles produced by amino acid sequences of Cas1 and Cas2
990 (https://web.expasy.org/protscale/). SP: signal peptide; red and black arrowheads show
991 the positions of the negatively and positively charged amino acids, respectively, in mature
992 domains; red and yellow rectangles show the regions in which the hydrophobicity and
993 secondary structure of Cas1 and Cas2 may differ. **Related to Figure 1 and Figure 1-**

table 1.

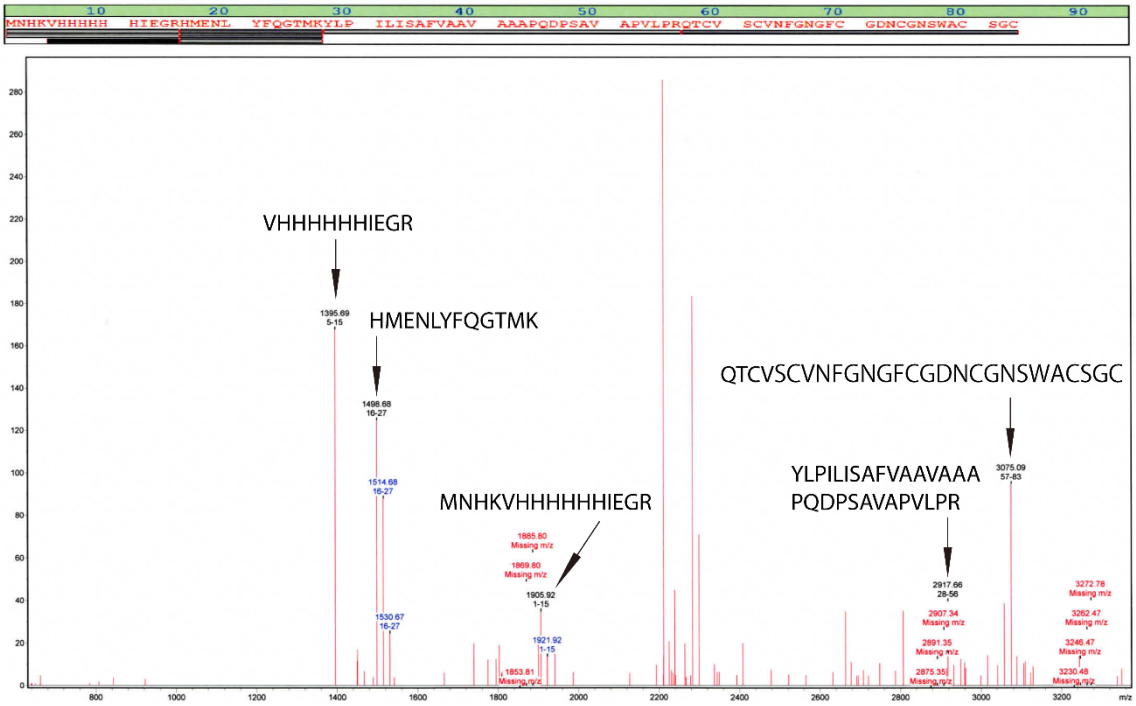

Figure 1-figure supplement 2. MALDI FT-ICR mass spectrometry of Cas1. The m/z signals in good agreement with the calculated mass are marked by the corresponding amino acid sequences. **<u>Related to Figure 1 and Figure 1-table 1</u>**.

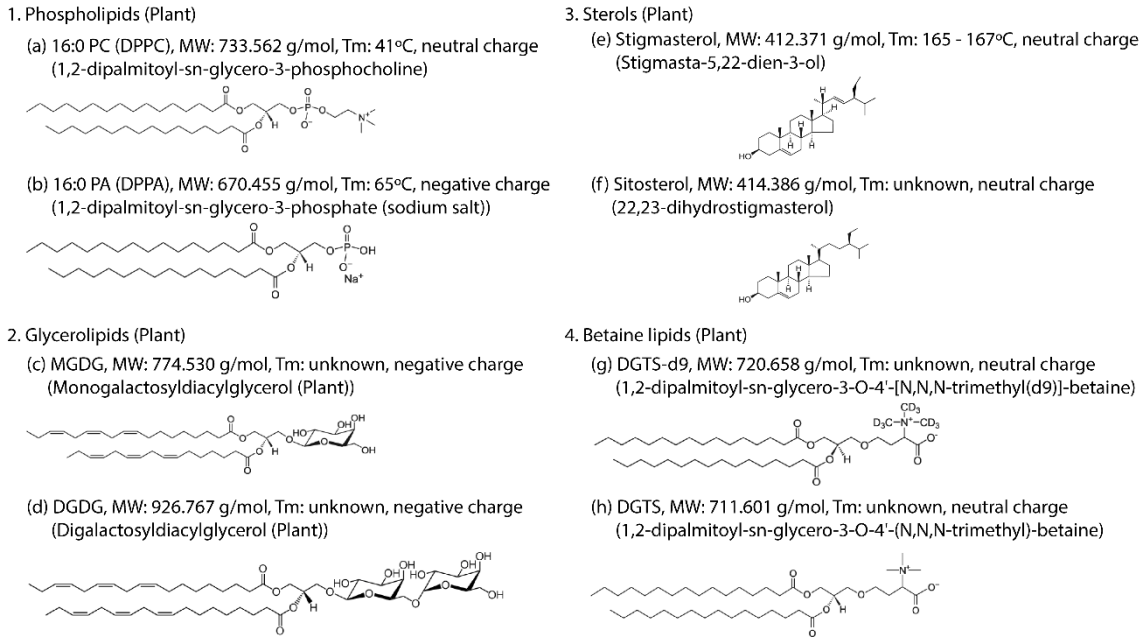

Figure 1-figure supplement 3. Structures and physical properties of different lipids available in cytoplasmic membranes of plant cells. Tm: melting temperature. Data were obtained from Avanti Polar Lipids (Alabama, USA). **<u>Related to Figures 1, 2, 3, and 4</u>**.

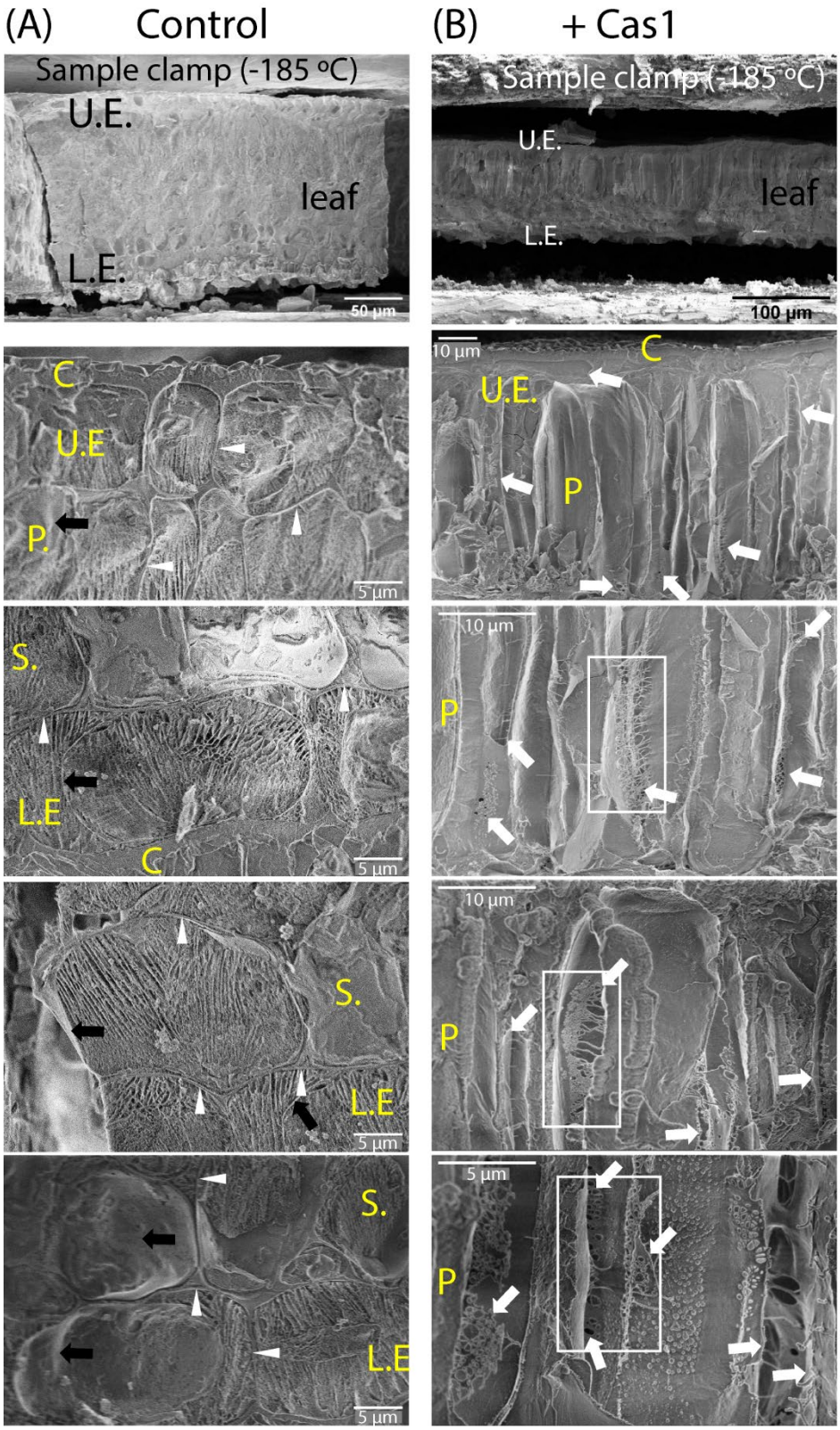

1075

1076 **Figure 6-figure supplement 1.** Cryo-SEM images of cellular and tissue structures of
1077 control and lesion spots in rubber leaves (rubber clone RRIV 4) caused by Cas1. Black

and white arrows denote healthy and unhealthy cytoplasmic membranes, respectively. White arrowheads denote the cell wall. C: cuticle; U.E.: upper epidermis; L.E.: lower epidermis; P.: palisade; S.: spongy. Rectangles denote biofilm-like structures of Cas1 formed on cytoplasmic membrane. **Related to Figure 6**.

1114 **Table supplements**

1115 **Figure 1-table 1**. Peptides predicted for and detected (red characters) by MALDI FT-ICR

1116 mass spectrometry. **Related to Figure 1-figure supplement 2**.

Peptide ID	Amino acid number	Predicted Mass	Number of uncleaved sites	Sequence and modifications
1	[1 – 4]	529.255	0	MNHK
1	[1 – 4]	545.250	0	MNHK (1 * Oxidation (M))
2	[1 – 15]	1905.926	1	MNHKVHHHHHHHIEGR
2	[1 – 15]	1921.921	1	MNHKVHHHHHHHIEGR (1 * Oxidation (M))
3	[1 – 27]	3385.590	2	MNHKVHHHHHHHIEGR HMENLYFQGTMK
3	[1 – 27]	3401.585	2	MNHKVHHHHHHHIEGR HMENLYFQGTMK (1 * Oxidation (M))
3	[1 – 27]	3417.580	2	MNHKVHHHHHHHIEGR HMENLYFQGTMK (2 * Oxidation (M))
3	[1 – 27]	3433.575	2	MNHKVHHHHHHHIEGR HMENLYFQGTMK (3 * Oxidation (M))
4	[5 – 15]	1395.689	0	VHHHHHHHIEGR
5	[5 – 27]	2875.353	1	VHHHHHHHIEGRHMENLYFQGTMK
5	[5 – 27]	2891.348	1	VHHHHHHHIEGRHMENLYFQGTMK (1 * Oxidation (M))
5	[5 – 27]	2907.343	1	VHHHHHHHIEGRHMENLYFQGTMK (2 * Oxidation (M))
7	[16 – 27]	1498.682	0	HMENLYFQGTMK
7	[16 – 27]	1514.677	0	HMENLYFQGTMK (1 * Oxidation (M))
7	[16 – 27]	1530.672	0	HMENLYFQGTMK (2 * Oxidation (M))

8	[16 – 56]	4397.319	1	HMENLYFQGTMKYLPILISAFVAAVAAAPQDPSAVAPVLPR
8	[16 – 56]	4413.314	1	HMENLYFQGTMKYLPILISAFVAAVAAAPQDPSAVAPVLPR (1 * Oxidation (M))
8	[16 – 56]	4429.309	1	HMENLYFQGTMKYLPILISAFVAAVAAAPQDPSAVAPVLPR (2 * Oxidation (M))
10	[28 – 56]	2917.655	0	YLPILISAFVAAVAAAPQDPSAVAPVLPR
12	[57 – 83]	3075.100	0	QTCVSCVNFGNGFCGDNCGNSWACSGC (6 * Carbamidomethyl (C))

1140 **Figure 1-table 2.** Information on oligonucleotide sequences of genes encoding Cas1 and
1141 Cas2 and amino acid sequences of recombinant Cas1, Cas2, GFP-Cas1, and GFP-Cas2
1142 proteins. We explain amino acid sequences in Cas1 and Cas2; bold letters are full-length
1143 Cas1 and Cas2 proteins, in which the signal peptides are underlined letters followed by
1144 the putative mature domains. The italic letters indicate a 6xHis-tag followed by the amino
1145 acid linker on the N-terminal domain of Cas1 and Cas2 for purifying these recombinant
1146 proteins. For GFP-Cas1 and GFP-Cas2, bold letters are a fusion of GFP (underlined and
1147 bold letters) with Cas1 or Cas2 (bold letters). The italic letters indicate a 6xHis-tag
1148 followed by the amino acid linker. **Related to Figure 1-figure supplement 1.**

Cas1 GenBank: ABV25895	5'atgaaatatctccctatcctcatctctgcttttgtagcagccgttgctgcagcccc gcaagatccgtctgctgtggcacctgtactccctagacagacttgcgtaagctgtg tcaatttcggcaatgggttttgtggcgataactgtggtaattcttgggcttgttcggga tgttaa3'
Cas2 GenBank: ADC54229	5'atgaaatacctccctatcttcatctctgcttttgtagcagccgttgctgcagttccg cagggtccgtctgctgcggcagcagctattcttcctagacagtcttgcgtatcatgt gtcgatttcggcaacgggttctgtggcgacaactgtggtaattcctgggcttgttcg ggttgttag3'
FWCas1 primer (KpnI) FWGFP-Cas1 primer (in-fusion)	5' GGTACCatgaaatatctccctatcc 3' 5' ACTATACGGTGGATCCatgaaatatctccctatcct 3'
RVCas1 primer (XbaI) RVGFP-Cas1 primer (in-fusion)	5' TCTAGAttaacatcccgaacaagcc 3' 5' ACTATACGGTGGATCCatgaaatatctccctatcct 3'
FWCas2 primer (KpnI) FWGFP-Cas2 primer (in-fusion)	5' GGTACCatgaaatacctccctatct 3' 5' ACTATACGGTGGATCCatgaaatacctccctatct 3'
RVCas2 primer (XbaI) RVGFP-Cas2 primer (in-fusion)	5' TCTAGActaacaacccgaacaagc 3' 5' GCAGGTCGACAAGCTTctaacaacccgaacaag 3'
Cas1, 83 amino acids, 9003.27 Da	*M N H K V H H H H H H I E G R H M E N L Y F Q G T* **M K Y L P I L I S A F V A A V A A A P Q D P S A V A P V L P R Q T C V S C V N F G N G F C G D N C G N S W A C S G C ***
Cas2, 84 amino acids, 9025.28 Da	*M N H K V H H H H H H I E G R H M E N L Y F Q G T* **M K Y L P I F I S A F V A A V A A V P Q G P S A A A A A I L P R Q S C V S C V D F G N G F C G D N C G N S W**

	A C S G C *
GFP-Cas1, 319 amino acids, 35400.95 KDa	*M N H K V H H H H H H I E G R H M E L G T* **M S K G E E L F T G V V P I L V E L D G** -------- **F G N G F C G D N C G N S W A C S G C ***
GFP-Cas2, 320 amino acids, 35422.07 KDa	*M N H K V H H H H H H I E G R H M E L G T* **M S K G E E L F T G V V P I L V E L D G** -------- **D F G N G F C G D N C G N S W A C S G C ***

1178 **Figure 4-table 1.** Lipid compositions for making composite giant liposome vesicles
1179 (GVs). Because the composite GVs contain both giant multilamellar vesicles (GMVs)
1180 and giant unilamellar vesicles (GUVs), we therefore use these composite giant vesicles
1181 as GVs. **Related to Figure 4**

GVs	**DPPC**	**DPPC/ DPPA**	**DPPC/ MGDG**	**DPPC/ DGDG**	**DPPC/ Stigmasterol**	**DPPC/ Sitosterol**	**DPPC/ DGTS-d9**	**DPPC/ DGTS**
DPPC	10 mM	8 mM	7.5 mM	7.5 mM	9 mM	9 mM	7.5 mM	7.5 mM
DPPA		2 mM						
MGDG			2.5 mM					
DGDG				2.5 mM				
Stimasterol					1 mM			
Sitosterol						1 mM		
DGTS-d9							2.5 mM	
DGTS								2.5 mM
18:1 Liss Rhod PE	0.1 mM	0.1 mM	0.1 mM	0.1 mM	0.1 mM	0.1 mM	0.1 mM	0.1 mM
16:0 Biotinyl PE	0.5 mM	0.5 mM	0.5 mM	0.5 mM	0.5 mM	0.5 mM	0.5 mM	0.5 mM

1182
1183
1184
1185
1186
1187
1188
1189
1190
1191
1192
1193
1194
1195
1196

1197 **Video supplements**

1198 **Video 1**. Disruption of DPPC membrane lipids caused by Cas1. Briefly, DPPC lipid
1199 bilayers were formed on mica by rupturing DPPC liposomes. Then, 0.95 μM Cas1 was
1200 added, and HS-AFM imaging was carried out in C-buffer using BL-AC10DS-A2
1201 cantilever deposited with a small Lab-made tip. AFM imaging rate: 2 fps. The Video plays
1202 at 30 fps. Bars: 50 nm. **Related to Figure 1a1, Figure 1-figure supplement 3, and Table**
1203 **1**.

1204 **Video 2**. Disruption of DPPC membrane lipids caused by Cas2. Briefly, DPPC lipid
1205 bilayers were formed on mica by rupturing DPPC liposomes. Then, 0.95 μM Cas2 was
1206 added, and HS-AFM imaging was carried out in C-buffer using BL-AC10DS-A2
1207 cantilever deposited with a small Lab-made tip. AFM imaging rate: 2 fps. The Video plays
1208 at 30 fps. Bars: 50 nm. **Related to Figure 1a2, Figure 1-figure supplement 3, and Table**
1209 **1**.

1210 **Video 3**. Disruption of DPPC/DPPA membrane lipids caused by Cas1. Briefly,
1211 DPPC/DPPA (85/20 wt%) lipid bilayers were formed on mica by rupturing DPPC/DPPA
1212 liposomes. Then, 0.95 μM Cas1 was added, and HS-AFM imaging was carried out in C-
1213 buffer using BL-AC10DS-A2 cantilever deposited with a small Lab-made tip. AFM
1214 imaging rate: 2 fps. The Video plays at 30 fps. Bars: 50 nm. **Related to Figure 1b1,**
1215 **Figure 1-figure supplement 3, and Table 1**.

1216 **Video 4**. Disruption of DPPC/DPPA membrane lipids caused by Cas2. Briefly,
1217 DPPC/DPPA (85/20 wt%) lipid bilayers were formed on mica by rupturing DPPC/DPPA
1218 liposomes. Then, 0.95 μM Cas2 was added, and HS-AFM imaging was carried out in C-
1219 buffer using BL-AC10DS-A2 cantilever deposited with a small Lab-made tip. AFM
1220 imaging rate: 2 fps. The Video plays at 30 fps. Bars: 50 nm. **Related to Figure 1b2,**
1221 **Figure 1-figure supplement 3, and Table 1**.

1222 **Video 5**. Disruption of DPPC/MGDG membrane lipids caused by Cas1. Briefly,
1223 DPPC/MGDG (80/20 wt%) lipid bilayers were formed on mica by rupturing
1224 DPPC/MGDG liposomes. Then, 0.95 μM Cas1 was added, and HS-AFM imaging was
1225 carried out in C-buffer using BL-AC10DS-A2 cantilever deposited with a small Lab-
1226 made tip. AFM imaging rate: 2 fps. The Video plays at 30 fps. Bars: 50 nm. **Related to**
1227 **Figure 1c1, Figure 1-figure supplement 3, and Table 1**.

1228 **Video 6**. Disruption of DPPC/MGDG membrane lipids caused by Cas2. Briefly,
1229 DPPC/MGDG (80/20 wt%) lipid bilayers were formed on mica by rupturing
1230 DPPC/MGDG liposomes. Then, 0.95 μM Cas2 was added, and HS-AFM imaging was
1231 carried out in C-buffer using BL-AC10DS-A2 cantilever deposited with a small Lab-
1232 made tip. AFM imaging rate: 2 fps. The Video plays at 30 fps. Bars: 50 nm. **Related to**

1233 **Figure 1c2, Figure 1-figure supplement 3, and Table 1**.
1234 **Video 7**. Disruption of DPPC/DGDG membrane lipids caused by Cas1. Briefly,
1235 DPPC/DGDG (60/40 wt%) lipid bilayers were formed on mica by rupturing
1236 DPPC/DGDG liposomes. Then, 0.95 μM Cas1 was added, and HS-AFM imaging was
1237 carried out in C-buffer using BL-AC10DS-A2 cantilever deposited with a small Lab-
1238 made tip. AFM imaging rate: 2 fps. The Video plays at 30 fps. Bars: 50 nm. **Related to**
1239 **Figure 1d1, Figure 1-figure supplement 3, and Table 1**.
1240 **Video 8**. Disruption of DPPC/DGDG membrane lipids caused by Cas2. Briefly,
1241 DPPC/DGDG (60/40 wt%) lipid bilayers were formed on mica by rupturing
1242 DPPC/DGDG liposomes. Then, 0.95 μM Cas2 was added, and HS-AFM imaging was
1243 carried out in C-buffer using BL-AC10DS-A2 cantilever deposited with a small Lab-
1244 made tip. AFM imaging rate: 2 fps. The Video plays at 30 fps. Bars: 50 nm. **Related to**
1245 **Figure 1d2, Figure 1-figure supplement 3, and Table 1**.
1246 **Video 9**. Disruption of DPPC/stigmasterol membrane lipids caused by Cas1. Briefly,
1247 DPPC/stigmasterol (80/20 wt%) lipid bilayers were formed on mica by rupturing
1248 DPPC/stigmasterol liposomes. Then, 0.95 μM Cas1 was added, and HS-AFM imaging
1249 was carried out in C-buffer using BL-AC10DS-A2 cantilever deposited with a small Lab-
1250 made tip. AFM imaging rate: 2 fps. The Video plays at 30 fps. Bars: 50 nm. **Related to**
1251 **Figure 1e1, Figure 1-figure supplement 3, and Table 1**.
1252 **Video 10**. Disruption of DPPC/stigmasterol membrane lipids caused by Cas2. Briefly,
1253 DPPC/stigmasterol (80/20 wt%) lipid bilayers were formed on mica by rupturing
1254 DPPC/stigmasterol liposomes. Then, 0.95 μM Cas2 was added, and HS-AFM imaging
1255 was carried out in C-buffer using BL-AC10DS-A2 cantilever deposited with a small Lab-
1256 made tip. AFM imaging rate: 2 fps. The Video plays at 30 fps. Bars: 50 nm. **Related to**
1257 **Figure 1e2, Figure 1-figure supplement 3, and Table 1**.
1258 **Video 11**. Disruption of DPPC/sitosterol membrane lipids caused by Cas1. Briefly,
1259 DPPC/sitosterol (80/20 wt%) lipid bilayers were formed on mica by rupturing
1260 DPPC/Sitosterol liposomes. Then, 0.95 μM Cas1 was added, and HS-AFM imaging was
1261 carried out in C-buffer using BL-AC10DS-A2 cantilever deposited with a small Lab-
1262 made tip. AFM imaging rate: 2 fps. The Video plays at 30 fps. Bars: 50 nm. **Related to**
1263 **Figure 1f1, Figure 1-figure supplement 3, and Table 1**.
1264 **Video 12**. Disruption of DPPC/sitosterol membrane lipids caused by Cas2. Briefly,
1265 DPPC/sitosterol (80/20 wt%) lipid bilayers were formed on mica by rupturing
1266 DPPC/Sitosterol liposomes. Then, 0.95 μM Cas2 was added, and HS-AFM imaging was
1267 carried out in C-buffer using BL-AC10DS-A2 cantilever deposited with a small Lab-
1268 made tip. AFM imaging rate: 2 fps. The Video plays at 30 fps. Bars: 50 nm. **Related to**

1269 **Figure 1f2, Figure 1-figure supplement 3, and Table 1**.
1270 **Video 13**. Disruption of DPPC/DGTS-d9 membrane lipids caused by Cas1. Briefly,
1271 DPPC/DGTS-d9 (80/20 wt%) lipid bilayers were formed on mica by rupturing
1272 DPPC/DGTS-d9 liposomes. Then, 0.95 μM Cas1 was added, and HS-AFM imaging was
1273 carried out in C-buffer using BL-AC10DS-A2 cantilever deposited with a small Lab-
1274 made tip. AFM imaging rate: 2 fps. The Video plays at 30 fps. Bars: 50 nm. **Related to**
1275 **Figure 1g1, Figure 1-figure supplement 3, and Table 1**.
1276 **Video 14**. Disruption of DPPC/DGTS-d9 membrane lipids caused by Cas2. Briefly,
1277 DPPC/DGTS-d9 (80/20 wt%) lipid bilayers were formed on mica by rupturing
1278 DPPC/DGTS-d9 liposomes. Then, 0.95 μM Cas2 was added, and HS-AFM imaging was
1279 carried out in C-buffer using BL-AC10DS-A2 cantilever deposited with a small Lab-
1280 made tip. AFM imaging rate: 2 fps. The Video plays at 30 fps. Bars: 50 nm. **Related to**
1281 **Figure 1g2, Figure 1-figure supplement 3, and Table 1**.
1282 **Video 15**. Disruption of DPPC/DGTS membrane lipids caused by Cas1. Briefly,
1283 DPPC/DGTS (80/20 wt%) lipid bilayers were formed on mica by rupturing DPPC/DGTS
1284 liposomes. Then, 0.95 μM Cas1 was added, and HS-AFM imaging was carried out in C-
1285 buffer using BL-AC10DS-A2 cantilever deposited with a small Lab-made tip. AFM
1286 imaging rate: 2 fps. The Video plays at 30 fps. Bars: 50 nm. **Related to Figure 1h1,**
1287 **Figure 1-figure supplement 3, and Table 1**.
1288 **Video 16**. Disruption of DPPC/DGTS membrane lipids caused by Cas2. Briefly,
1289 DPPC/DGTS (80/20 wt%) lipid bilayers were formed on mica by rupturing DPPC/DGTS
1290 liposomes. Then, 0.95 μM Cas2 was added, and HS-AFM imaging was carried out in C-
1291 buffer using BL-AC10DS-A2 cantilever deposited with a small Lab-made tip. AFM
1292 imaging rate: 2 fps. The Video plays at 30 fps. Bars: 50 nm. **Related to Figure 1h2,**
1293 **Figure 1-figure supplement 3, and Table 1**.
1294 **Video 17**. Biofilm-like formation of Cas1/Cas2 mixtures onto DPPC/sitosterol
1295 membranes. Briefly, DPPC/sitosterol (80/20 wt%) lipid bilayers were formed on mica by
1296 rupturing DPPC/sitosterol liposomes. Then, 4.75 μM Cas1 and 4.75 μM Cas2 were added,
1297 and HS-AFM imaging was carried out in C-buffer using BL-AC10DS-A2 cantilever
1298 deposited with a small Lab-made tip. AFM imaging rate: 2 fps. The Video plays at 30 fps.
1299 Bars: 50 nm. **Related to Figure 3A.**
1300 **Video 18**. Biofilm-like formation of Cas2 onto DPPC/sitosterol membranes. Briefly,
1301 DPPC/sitosterol (80/20 wt%) lipid bilayers were formed on mica by rupturing
1302 DPPC/sitosterol liposomes. Then, 4.75 μM Cas2 was added, and HS-AFM imaging was
1303 carried out in C-buffer using BL-AC10DS-A2 cantilever deposited with a small Lab-
1304 made tip. AFM imaging rate: 2 fps. The Video plays at 30 fps. Bars: 50 nm. **Related to**

1305 **Figure 3B**.
1306 **Video 19**. Biofilm-like structures of Cas1/Cas2 mixtures were not formed onto
1307 DPPC/DGTS-d9 membranes. Briefly, DPPC/DGTS-d9 (80/20 wt%) lipid bilayers were
1308 formed on mica by rupturing DPPC/DGTS-d9 liposomes. Then, 4.75 µM Cas1 and 4.75
1309 µM Cas2 were added, and HS-AFM imaging was carried out in C-buffer using BL-
1310 AC10DS-A2 cantilever deposited with a small Lab-made tip. AFM imaging rate: 2 fps.
1311 The Video plays at 30 fps. Bars: 50 nm. **Related to Figure 3C.**
1312
1313
1314
1315
1316
1317
1318
1319
1320
1321
1322
1323
1324
1325
1326
1327
1328
1329
1330
1331
1332
1333
1334
1335
1336
1337
1338
1339
1340

References

Ando T. 2018. High-speed atomic force microscopy and its future prospects. *Biophys Rev* **10**:285–292. doi:10.1007/s12551-017-0356-5

Ando T. 2012. High-speed atomic force microscopy coming of age. *Nanotechnology* **23**:1–27. doi:10.1088/0957-4484/23/6/062001

Ando T, Uchihashi T, Fukuma T. 2008. High-speed atomic force microscopy for nano-visualization of dynamic biomolecular processes. *Prog Surf Sci* **83**:337–437. doi:10.1016/j.progsurf.2008.09.001

Ando T, Uchihashi T, Kodera N. 2013. High-Speed AFM and Applications to Biomolecular Systems. *Annu Rev Biophys* **42**:393–414. doi:10.1146/annurev-biophys-083012-130324

Ando T, Uchihashi T, Kodera N, Yamamoto D, Taniguchi M, Miyagi A, Yamashita H. 2007. High-speed Atomic Force Microscopy for Nano-visualization of Biomolecular Processes. *J Mol Recognit* **20**:448–458. doi:10.1002/9783527626137.ch12

Angelova M, Dimitrov DS. 2007. A mechanism of liposome electroformation. *Trends Colloid Interface Sci II* **76**:59–67. doi:10.1007/bfb0114171

Angelova MI, Dimitrov DS. 1986. Liposome Electroformation. *Faraday Discuss Chem Soc* **81**:303–311.

Assmann SM, Haubrick LL. 1996. Transport proteins of the plant plasma membrane. *Curr Opin Cell Biol* **8**:458–467. doi:10.1016/S0955-0674(96)80021-4

Bae SW, Jung S, Choi SC, Kim MY, Ryu SB. 2020. Lipid Composition of Latex and Rubber Particlesin *Hevea brasiliensis* and *Taraxacum kok-saghyz*. *molecules* **25**:1–13. doi:10.3390/molecules25215110

Barthe P, Pujade-Renaud V, Breton F, Gargani D, Thai R, Roumestand C, de Lamotte F. 2007. Structural Analysis of Cassiicolin, a Host-selective Protein Toxin from *Corynespora cassiicola*. *J Mol Biol* **367**:89–101. doi:10.1016/j.jmb.2006.11.086

Carvalho K, Ramos L, Roy C, Picart C. 2008. Giant unilamellar vesicles containing phosphatidylinositol(4,5) bisphosphate: Characterization and functionality. *Biophys J* **95**:4348–4360. doi:10.1529/biophysj.107.126912

de Lamotte F, Duviau MP, Sanier C, Thai R, Poncet J, Bieysse D, Breton F, Pujade-Renaud V. 2007. Purification and characterization of cassiicolin, the toxin produced by *Corynespora cassiicola*, causal agent of the leaf fall disease of rubber tree. *J Chromatogr B Anal Technol Biomed Life Sci* **849**:357–362. doi:10.1016/j.jchromb.2006.10.051

Déon M, Bourré Y, Gimenez S, Berger A, Bieysse D, De Lamotte F, Poncet J, Roussel V, Bonnot F, Oliver G, Franchel J, Seguin M, Leroy T, Roeckel-Drevet P, Pujade-

1377 Renaud V. 2012a. Characterization of a cassiicolin-encoding gene from *Corynespora*
1378 *cassiicola*, pathogen of rubber tree (*Hevea brasiliensis*). *Plant Sci* **185–186**:227–237.
1379 doi:10.1016/j.plantsci.2011.10.017
1380 Déon M, Fumanal B, Gimenez S, Bieysse D, Oliveira RR, Shuib SS, Breton F,
1381 Sunderasan E, Vida JB, Seguin M, Leroy T, Roeckel-Drevet P, Pujade-Renaud V.
1382 2014. Diversity of the cassiicolin gene in *Corynespora cassiicola* and relation with
1383 the pathogenicity in *Hevea brasiliensis*. *Fungal Biol* **118**:32–47.
1384 doi:10.1016/j.funbio.2013.10.011
1385 Déon M, Scomparin A, Tixier A, Mattos CRR, Leroy T, Seguin M, Roeckel-Drevet P,
1386 Pujade-Renaud V. 2012b. First characterization of endophytic *Corynespora*
1387 *cassiicola* isolates with variant cassiicolin genes recovered from rubber trees in
1388 Brazil. *Fungal Divers*. doi:10.1007/s13225-012-0169-6
1389 Dimitrov DS, Angelova MI. 1988. Lipid swelling and liposome formation mediated by
1390 electric fields. *Bioelectrochemistry Bioenerg* **19**:323–336. doi:10.1016/0302-
1391 4598(88)80013-8
1392 Dixon LJ, Schlub RL, Pernezny K, Datnoff LE. 2009. Host specialization and
1393 phylogenetic diversity of *Corynespora cassiicola*. *Phytopathology* **99**:1015–1027.
1394 doi:10.1094/PHYTO-99-9-1015
1395 Dörmann P, Benning C. 2002. Galactolipids rule in seed plants. *Trends Plant Sci* **7**:112–
1396 118. doi:10.1016/S1360-1385(01)02216-6
1397 Drücker P, Iacovache I, Bachler S, Zuber B, Babiychuk EB, Dittrich PS, Draeger A. 2019.
1398 Membrane deformation and layer-by-layer peeling of giant vesicles induced by the
1399 pore-forming toxin pneumolysin. *Biomater Sci* **7**:3693–3705.
1400 doi:10.1039/c9bm00134d
1401 Dufourc EJ. 2008a. Sterols and membrane dynamics. *J Chem Biol* **1**:63–77.
1402 doi:10.1007/s12154-008-0010-6
1403 Dufourc EJ. 2008b. The role of phytosterols in plant adaptation to temperature. *Plant*
1404 *Signal Behav* **3**:133–134. doi:10.4161/psb.3.2.5051
1405 Gour N, Ngo KX, Vebert-Nardin C. 2014. Anti-infectious surfaces achieved by polymer
1406 modification. *Macromol Mater Eng* **299**:648–668. doi:10.1002/mame.201300285
1407 Hartmann MA. 1998. Plant sterols and the membrane environment. *Trends Plant Sci*
1408 **3**:170–175. doi:10.1016/S1360-1385(98)01233-3
1409 Heath GR, Scheuring S. 2019. Advances in high-speed atomic force microscopy (HS-
1410 AFM) reveal dynamics of transmembrane channels and transporters. *Curr Opin*
1411 *Struct Biol* **57**:93–102. doi:10.1016/j.sbi.2019.02.008
1412 Hellman U, Wernstedt C, Gonez J, Heldin C-H. 1995. Improvement of an “In-Gel”

1413 Digestion Procedure for the Micropreparation of Internal Protein Fragments for
1414 Amino Acid Sequencing. *Anal Biochem* **224**:451–455.
1415 Hieu ND, Nghia NA, Uyen NTK, Chau NNB, Quoc NB. 2020. Genetic diversity analysis
1416 of *Corynespora cassiicola* isolates on the rubber tree (*Hevea brasiliensis*) in Vietnam
1417 using ribosomal DNA internal transcribed spacer (rDNA-ITS) sequences and
1418 sequence-related amplified polymorphism (SRAP). *J Rubber Res* **23**:173–185.
1419 doi:10.1007/s42464-020-00047-7
1420 Kang J, Park J, Choi H, Burla B, Kretzschmar T, Lee Y, Martinoia E. 2011. Plant ABC
1421 Transporters. *Arab B* **9**:e0153. doi:10.1199/tab.0153
1422 Karner A, Nimmervoll B, Plochberger B, Klotzsch E, Horner A, Knyazev DG, Kuttner R,
1423 Winkler K, Winter L, Siligan C, Ollinger N, Pohl P, Preiner J. 2017. Tuning
1424 membrane protein mobility by confinement into nanodomains. *Nat Nanotechnol*
1425 **12**:260–266. doi:10.1038/nnano.2016.236
1426 Kawakita Y, Kinoshita M, Furukawa Y, Tulum I, Tahara YO, Katayama E, Namba K,
1427 Miyata M. 2016. Structural study of MPN387, an essential protein for gliding
1428 motility of a human-pathogenic bacterium, *Mycoplasma pneumoniae*. *J Bacteriol*
1429 **198**:2352–2359. doi:10.1128/JB.00160-16
1430 Kodera N, Noshiro D, Dora SK, Mori T, Habchi J, Blocquel D, Gruet A, Dosnon M,
1431 Salladini E, Bignon C, Fujioka Y, Oda T, Noda NN, Sato M, Lotti M, Mizuguchi M,
1432 Longhi S, Ando T. 2020. Structural and dynamics analysis of intrinsically disordered
1433 proteins by high-speed atomic force microscopy. *Nat Nanotechnol*.
1434 doi:10.1038/s41565-020-00798-9
1435 Kodera N, Yamamoto D, Ishikawa R, Ando T. 2010. Video imaging of walking myosin V
1436 by high-speed atomic force microscopy. *Nature* **468**:72–76.
1437 doi:10.1038/nature09450
1438 Liengprayoon S, Sriroth K, Dubreucq E, Vaysse L. 2011. Glycolipid composition of
1439 *Hevea brasiliensis* latex. *Phytochemistry* **72**:1902–1913.
1440 doi:10.1016/j.phytochem.2011.04.023
1441 Lin YC, Chipot C, Scheuring S. 2020. Annexin-V stabilizes membrane defects by
1442 inducing lipid phase transition. *Nat Commun* **11**:1–13. doi:10.1038/s41467-019-
1443 14045-w
1444 Lopez D, Ribeiro S, Label P, Fumanal B, Venisse JS, Kohler A, de Oliveira RR, Labutti
1445 K, Lipzen A, Lail K, Bauer D, Ohm RA, Barry KW, Spatafora J, Grigoriev I V.,
1446 Martin FM, Pujade-Renaud V. 2018. Genome-wide analysis of *Corynespora*
1447 *cassiicola* leaf fall disease putative effectors. *Front Microbiol* **9**:1–21.
1448 doi:10.3389/fmicb.2018.00276

1449 Mackender RO, Leech RM. 1974. The Galactolipid, Phospholipid, and Fatty Acid
1450 Composition of the Chloroplast Envelope Membranes of *Vicia faba . L. . Plant*
1451 *Physiol* **53**:496–502. doi:10.1104/pp.53.3.496
1452 Mancera E, Nocedal I, Hammel S, Gulati M, Mitchell KF, Andes DR, Nobile CJ, Butler
1453 G, Johnson AD. 2020. Evolution of the complex transcription network controlling
1454 biofilm formation in *Candida species*. *bioRxiv*. doi:10.1101/2020.11.08.373514
1455 Maure C, Verdoucq L, Luu DT, Santoni V. 2008. Plant aquaporins: Membrane channels
1456 with multiple integrated functions. *Annu Rev Plant Biol* **59**:595–624.
1457 doi:10.1146/annurev.arplant.59.032607.092734
1458 Meena M, Samal S. 2019. *Alternaria* host-specific (HSTs) toxins: An overview of
1459 chemical characterization, target sites, regulation and their toxic effects. *Toxicol*
1460 *Reports* **6**:745–758. doi:10.1016/j.toxrep.2019.06.021
1461 Murakami H, Nobusawa T, Hori K, Shimojima M, Ohta H. 2018. Betaine lipid is crucial
1462 for adapting to low temperature and phosphate deficiency in nannochloropsis. *Plant*
1463 *Physiol* **177**:181–193. doi:10.1104/pp.17.01573
1464 Nasrallah H, Vial A, Nicolas P, Soulier J, Costa L, Godefroy C, Bourillot E, Lesniewska
1465 E, Milhiet P-E, Affiliations. 2019. Imaging Artificial Membranes Using High-Speed
1466 Atomic Force Microscopy. *Methods Mol Biol* **1886**:45–59. doi:10.1007/978-1-4939-
1467 8894-5_3
1468 Nghia NA, Kadir J, Sunderasan E, Puad Abdullah M, Malik A, Napis S. 2008.
1469 Morphological and Inter Simple Sequence Repeat (ISSR) markers analyses of
1470 Corynespora cassiicola isolates from rubber plantations in Malaysia.
1471 *Mycopathologia* **166**:189–201. doi:10.1007/s11046-008-9138-8
1472 Ngo KX, Kodera N, Katayama E, Ando T, Uyeda TQ. 2015. Cofilin-induced
1473 unidirectional cooperative conformational changes in actin filaments revealed by
1474 high-speed atomic force microscopy. *Elife* **4**:e04806. doi:10.7554/eLife.04806
1475 Nguyen HD, Nguyen NA, Vu CTQ, Phan DA. 2014. Genetic Diversity and Pathogenicity
1476 of *Corynespora cassiicola* Isolates from Rubber Trees and Other Hosts in Vietnam.
1477 *J Rubber Res* **17**:187–203.
1478 Osumi M, Konomi M, Sugawara T, Takagi T, Baba M. 2006. High-pressure freezing is a
1479 powerful tool for visualization of *Schizosaccharomyces pombe* cells: Ultra-low
1480 temperature and low-voltage scanning electron microscopy and immunoelectron
1481 microscopy. *J Electron Microsc (Tokyo)* **55**:75–88. doi:10.1093/jmicro/dfl014
1482 Park P, Fukutomi M, Akai S, Nishimura S. 1976. Effect of the host-specific toxin from
1483 *Alternaria kikuchiana* on the ultrastructure of plasma membranes of cells in leaves
1484 of Japanese pear. *Physiol Plant Pathol* **9**:167–174. doi:10.1016/0048-

4059(76)90036-9

Petrov V, Qureshi MK, Hille J, Gechev T. 2018. Occurrence, biochemistry and biological effects of host-selective plant mycotoxins. *Food Chem Toxicol* **112**:251–264. doi:10.1016/j.fct.2017.12.047

Poincelot RP. 1976. Lipid and Fatty Acid Composition of Chloroplast Envelope Membranes from Species with Differing Net Photosynthesis. *Plant Physiol* **58**:595–598. doi:10.1104/pp.58.4.595

Ribeiro S, Tran DM, Déon M, Clément-Demange A, Garcia D, Soumahoro M, Masson A, Pujade-Renaud V. 2019. Gene deletion of *Corynespora cassiicola* cassiicolin Cas1 suppresses virulence in the rubber tree. *Fungal Genet Biol* **129**:101–114. doi:10.1016/j.fgb.2019.05.004

Riley RT, Wang E, Schroeder JJ, Smith ER, Plattner RD, Abbas N, Yoo HS, Merrill AH. 1996. Evidence for disruption of sphingolipid metabolism as a contributing factor in the toxicity and carcinogenicity of fumonisins. *Nat Toxins* **4**:3–15. doi:10.1002/19960401NT2

Roy CB, Liu H, Rajamani A, Saha T. 2019. Transcriptome profiling reveals genetic basis of disease resistance against *Corynespora cassiicola* in rubber tree (*Hevea brasiliensis*). *Curr Plant Biol* **17**:2–16. doi:10.1016/j.cpb.2019.02.002

Shibata M, Nishimasu H, Kodera N, Hirano S, Ando T, Uchihashi T, Nureki O. 2017. Real-space and real-time dynamics of CRISPR-Cas9 visualized by high-speed atomic force microscopy. *Nat Commun* **8**:1–9. doi:10.1038/s41467-017-01466-8

Shrestha SK, Lamour K, Young-Kelly H. 2017. Genome sequences and SNP analyses of *Corynespora cassiicola* from cotton and soybean in the southeastern United States reveal limited diversity. *PLoS One* **12**:6–14. doi:10.1371/journal.pone.0184908

Siqueira VM, Lima N. 2013. Biofilm Formation by Filamentous Fungi Recovered from a Water System. *J Mycol* **2013**:1–9. doi:10.1155/2013/152941

Slier DJ, Goodrich-Tanrikulu M, Cornish K, Stafford AE, McKeon TA. 1997. Composition of rubber particles of *Hevea brasiliensis*, *Parthenium argentatum*, *Ficus elastica*, and *Euphorbia lactiflua* indicates unconventional surface structure. *Plant Physiol Biochem*.

Sumabat LG, Kemerait RC, Brewer MT. 2018. Phylogenetic diversity and host specialization of *Corynespora cassiicola* responsible for emerging target spot disease of cotton and other crops in the southeastern United States. *Phytopathology* **108**:892–901. doi:10.1094/PHYTO-12-17-0407-R

Takaoka S, Kurata M, Harimoto Y, Hatta R, Yamamoto M, Akimitsu K, Tsuge T. 2014. Complex regulation of secondary metabolism controlling pathogenicity in the

1521 phytopathogenic fungus *Alternaria alternata*. *New Phytol* **202**:1297–1309.
1522 doi:10.1111/nph.12754
1523 Thatcher LF, Anderson JP, Singh KB. 2005. Plant Defence Responses: What Have We
1524 Learnt From *Arabidopsis*? *Funct Plant Biol* **32**:1–19. doi:10.1071/FP04135
1525 Tran DM, Clément-Demange A, Déon M, Garcia D, Le Guen V, Clément-Vidal A,
1526 Soumahoro M, Masson A, Label P, Le MT, Pujade-Renaud V. 2016. Genetic
1527 determinism of sensitivity to *Corynespora cassiicola* exudates in rubber tree (*Hevea*
1528 *brasiliensis*). *PLoS One* **11**:1–25. doi:10.1371/journal.pone.0162807
1529 Tsuge T, Harimoto Y, Akimitsu K, Ohtani K, Kodama M, Akagi Y, Egusa M, Yamamoto
1530 M, Otani H. 2013. Host-selective toxins produced by the plant pathogenic fungus
1531 *Alternaria alternata*. *FEMS Microbiol Rev* **37**:44–66. doi:10.1111/j.1574-
1532 6976.2012.00350.x
1533 Uchihashi T, Iino R, Ando T, Noji H. 2011. High-Speed Atomic Force Microscopy
1534 Reveals Rotary Catalysis of Rotorless F1-ATPase. *Science* **333**:755–758.
1535 doi:https://doi.org/10.1126/science.1205510
1536 Uchihashi T, Kodera N, Ando T. 2012. Guide to video recording of structure dynamics
1537 and dynamic processes of proteins by high-speed atomic force microscopy. *Nat*
1538 *Protoc* **7**:1193–1206. doi:10.1038/nprot.2012.047
1539 Wu J, Xie X, Shi Y, Chai A, Wang Q, Li B. 2018. Variation of cassiicolin genes among
1540 Chinese isolates of *Corynespora cassiicola*. *J Microbiol* **56**:634–647.
1541 doi:10.1007/s12275-018-7497-5
1542